Monthly Notices
of the
ROYAL ASTRONOMICAL SOCIETY

MNRAS **443,** 41–57 (2014) doi:10.1093/mnras/stu1155

Deep NIR photometry of H I galaxies in the Zone of Avoidance

W. L. Williams,[1,2,3]★ R. C. Kraan-Korteweg[1] and P. A. Woudt[1]

[1]*Department of Astronomy, Astrophysics, Cosmology and Gravity Centre (ACGC), University of Cape Town, Private Bag X3, Rondebosch 7701, South Africa*
[2]*Leiden Observatory, University of Leiden, PO Box 9513, NL-2300 RA Leiden, the Netherlands*
[3]*Netherlands Institute for Radio Astronomy (ASTRON), PO Box 2, NL-7990AA, Dwingeloo, the Netherlands*

Accepted 2014 June 9. Received 2014 June 2; in original form 2014 January 15

ABSTRACT

Current studies of the peculiar velocity flow field in the local Universe are limited by either the lack of detection or accurate photometry for galaxies at low Galactic latitudes. The contribution to the dynamics of the Local Group of the largely unknown mass distribution in this 'Zone of Avoidance' (ZoA) remains controversial. We present here the results of a pilot project to obtain deep near-infrared (NIR) observations of galaxies detected in the systematic Parkes deep H I survey of the ZoA(HIZOA) – 578 galaxies with recession velocities out to 6000 km s^{-1} were observed with the 1.4 m InfraRed Survey Facility SIRIUS (Simultaneous InfraRed Imager for Unbiased Surveys) camera providing J, H and K_s imaging 2 mag deeper than 2MASS. After star subtraction, the resulting isophotal magnitudes and inclinations of ZoA galaxies are of sufficient accuracy (magnitude errors under 0.1 mag even at high extinction) to ultimately be used to determine cosmic flow fields 'in' the ZoA via the NIR Tully–Fisher relation. We further used the observed NIR colours to assess the ratio of the true extinction to the Diffuse Infrared Background Experiment/*IRAS* extinction deep into the dust layers of the Milky Way. The derived ratio was found to be 0.87 across the HIZOA survey region with no significant variation with Galactic latitude or longitude. This value is in excellent agreement with the completely independently derived factor of 0.86 by Schlafly & Finkbeiner based on Sloan data far away from the Milky Way.

Key words: surveys – dust, extinction – galaxies: photometry – infrared: galaxies.

1 INTRODUCTION

The mass density field in the local Universe can be inferred from the measured peculiar velocities of galaxies, independent of any a priori assumption about the bias between visible and dark matter (Bertschinger & Dekel 1989; Dekel, Bertschinger & Faber 1990; Dekel 1994). The determination of the peculiar velocity field requires large and uniform galaxy samples with high-fidelity redshift-independent distance measurements. However, peculiar velocity surveys are plagued by poor detection statistics in the Zone of Avoidance (ZoA) where the obscuring effects of dust and stars in the Milky Way prevent the identification of galaxies across 10–20 per cent of the sky (e.g. Kraan-Korteweg & Lahav 2000; Kraan-Korteweg 2005). This problem is usually circumvented by statistical interpolation of the mass distribution adjacent to the ZoA (e.g. Yahil et al. 1991; Lynden-Bell, Lahav & Burstein 1989; Lahav et al. 1994). However, some studies, such as those by Kolatt, Dekel & Lahav (1995) and Loeb & Narayan (2008), suggest that these interpolations are inadequate and require unknown mass distributions to satisfactorily explain the peculiar motion of the Local Group with respect to the cosmic microwave background (CMB). In contrast, other works do not require any missing mass distributions to account for the Local Group motion (e.g. Erdoğdu & Lahav 2009). Several dynamically important structures, including the Great Attractor (GA; Lynden-Bell et al. 1988) and Local Void (Tully & Fisher 1987), are known to reside within the ZoA, and remain poorly mapped. Indeed, it is still a contentious issue – 25 years after its discovery – whether the GA is at rest with respect to the CMB, or itself partakes in a flow towards more distant attractors like the Shapley Concentration, possibly in combination with the Horologium-Reticulum Supercluster (Hudson et al. 2004; Lavaux et al. 2010; Lavaux & Hudson 2011).

Until we understand the mass distribution in the nearby Universe, *including the ZoA*, we cannot properly resolve the controversial results on what fraction of the bulk flow is generated locally (within about ∼100 Mpc), and what fraction results from inhomogeneities on even larger scales (e.g. Hudson et al. 2004; Watkins, Feldman & Hudson 2009; Feldman, Watkins & Hudson 2010; Kashlinsky et al. 2010; Bilicki et al. 2011; Macaulay et al. 2011; Nusser & Davis 2011; Abate & Feldman 2012). A full census of the large-scale structures hidden behind the Milky Way, preferentially with a map

★ E-mail: wwilliams@strw.LeidenUniv.nl

of the underlying ZoA density field, respectively cosmic flow field, is an absolute necessity to warrant that uncertainties due to the ZoA do not perpetuate into deeper whole-sky survey results.

Blind H I surveys have been shown to be most effective at detecting gas-rich galaxies in the most obscured parts of the ZoA. The H I Parkes Deep Zone of Avoidance Survey (Henning, Kraan-Korteweg & Staveley-Smith 2005), conducted on the 64 m Parkes Radio Telescope in Australia,[1] detected over 1000 galaxies in the southern ZoA. With an exposure time five times longer than the H I Parkes All Sky Survey (HIPASS; Barnes et al. 2001), the average rms noise of the survey was 6 mJy beam^{-1}. It covered a velocity range of $-1200 < v < 12\,700$ km s^{-1} with a channel spacing of 13.2 km s^{-1}. The survey covered the entire southern ZoA visible from Parkes: $212^\circ \leq l \leq 36^\circ$, $|b| < 5^\circ$ (Henning et al. 2005), followed by an extension to the north $36^\circ < l < 52^\circ$ and $196^\circ < l < 212^\circ$, $|b| < 5^\circ$ (Northern Extension; Donley et al. 2005), with a later broadening of the width of the survey around the Galactic bulge of $332^\circ < l < 36^\circ$, $5^\circ < |b| < 10^\circ$ and $352^\circ < l < 24^\circ$, $10^\circ < b < 15^\circ$ (Galactic bulge extension; Shafi 2008). The H I observations reveal galaxies where both optical and near-infrared (NIR) surveys fail due to high extinction and high stellar density. In fact, the deep Parkes HIZOA survey region was chosen specifically to cover this otherwise impenetrable region of the sky.

Apart from the large-scale structures delineated by galaxies detected in H I, their distances can be determined through the relation between linewidth and luminosity (Tully & Fisher 1977), and therewith their peculiar velocities. Tully–Fisher (TF) distances require three observational parameters: a measure of the flux and inclination of the galaxy as well as a measure of the rotational speed of the galaxy. The latter is readily available from the H I linewidths, corrected for inclination obtained from the surface photometry, while the former can be determined directly through surface photometry. Several such large-scale TF projects have been conducted to study the dynamics in the local universe, including the SFI (e.g. Giovanelli et al. 1994), expanded to the SFI++ (Masters et al. 2006; Springob et al. 2007), the Kinematics of the Local Universe (KLUN; e.g. Bottinelli et al. 1992) and KLUN++ (Theureau et al. 2007).

More recently, the 2MASS Tully–Fisher (2MTF) project (Masters, Springob & Huchra 2008) has been launched with the goal to perform a whole-sky TF analysis based on a complete sample of 2MASS galaxies brighter than $K_s^o < 11.25$ mag within a volume delimited by $v < 10\,000$ km s^{-1}. The use of NIR photometry for the TF relation has several advantages over optical photometry (Aaronson, Huchra & Mould 1979).

(i) The extinction, both internal and Galactic, is significantly reduced in the NIR. This results in smaller uncertainties introduced by extinction corrections and more robust photometric measurements. Also, effects on the inclination due to extinction are minimized.

(ii) The spectral energy distribution of galaxies peaks in the NIR, where it is dominated by the old, red stellar population. The long-lived low-mass stars provide the best indicator of the total stellar mass which governs the kinematics of galaxies and is unperturbed by recent short-term star formation which may be significant at bluer wavelengths.

(iii) The distribution of old stars is smoother, resulting in a smooth light profile. This makes it easier to fit elliptical isophotes resulting in cleaner photometry.

[1] The Parkes telescope is part of the Australia Telescope which is funded by the Commonwealth of Australia for operation as a National Facility managed by CSIRO.

Most importantly for our efforts in unveiling the ZoA is the low extinction in the NIR, compared to shorter wavelengths. This makes the NIR TF relation most ideal for use in the ZoA. However, the 'whole-sky' 2MTF did exclude the innermost ZoA ($|b| < 5^\circ$), as did the preceding 2MASS Redshift Survey (Huchra et al. 2012) from which the 2MTF was extracted. The reason is twofold: it is notoriously hard to get redshifts of optically obscured galaxies, even if visible in the NIR; secondly, 2MASS is highly incomplete around the Galactic bulge area at these low latitudes, and therefore along most of the southern ZoA which encompasses the dynamically important local large-scale structures such as the GA and the Local Void.

The finalization of the deep Parkes HIZOA survey has finally managed to trace the missing large-scale structures in the southern ZoA – although sparsely – through the detection of the gas-rich galaxies. The remaining question is: can we also get accompanying NIR imaging for these galaxies to permit an NIR TF analysis? Only few of these galaxies have counterparts in 2MASS (about 20–30 per cent, depending on Galactic longitude), and these lack the depth and resolution to accurately measure their photometric parameters. Deep high-resolution NIR observations are, however, able to penetrate the dust and deblend foreground stars, making it possible to detect NIR counterparts for the H I-detected spiral galaxies and measure their magnitudes and inclinations. As a pilot project, we have therefore started an NIR follow-up survey of a substantial sample of the HIZOA galaxies across the entire southern Galactic plane, delimited by $v < 6000$ km s^{-1}. This paper presents the results of this survey. It is the first step of a larger ongoing campaign to map the large-scale structures along the full 360° circle of the ZoA (Henning et al., in preparation; Kraan-Korteweg et al., in preparation), and follow up with a ZoA-optimized NIR TF analysis (Said et al., in preparation), now that this pilot project has proved this to be a feasible approach.

This paper is organized as follows. Section 2 describes the NIR observations, data reduction and image calibration. In Section 3, we discuss the detection of galaxies in the images, the removal of foreground stars as well as the surface photometry and determination of photometric parameters. The catalogue is analysed and discussed in Section 4, including an analysis of the variation in extinction across the ZoA and a calibration of the Diffuse Infrared Background Experiment (DIRBE) extinction maps.

2 OBSERVATIONS AND REDUCTION

2.1 Observations

The imaging data were acquired with the Japanese InfraRed Survey Facility (IRSF), a 1.4 m Alt-Azimuth Cassegrain telescope situated at the South African Astronomical Observatory site in Sutherland, South Africa. The IRSF is equipped with the Simultaneous InfraRed Imager for Unbiased Surveys (SIRIUS) capable of simultaneous imaging in the three NIR bands J, H and K_s. The camera consists of three 1024 × 1024 pixel HgCdTe (HAWAII) arrays each with a gain of 5.5e$^-$/ADU and a read-out noise of 30e$^-$ (Nagashima et al. 1999; Nagayama et al. 2003), cooled to 80 K. The field of view is 7.7 arcmin × 7.7 arcmin and the pixel scale is 0.45 arcsec pixel^{-1}. The high resolution of the IRSF greatly helps in identifying and deblending foreground stars, allowing them to be removed more accurately and improving the surface photometry of galaxies. Based on previous experience with SIRIUS in the ZoA (Nagayama et al. 2004, 2006; Skelton, Woudt & Kraan-Korteweg 2009; Riad 2010), each target field was observed with 25 frames of 24 s, resulting in an

Table 1. Summary of IRSF/SIRIUS observations.

Year	Month(s)	Fields	Observer(s)[a]
2006	March–June	7	NWS
2007	March–May	50	NS/JT/NWS
2007	August/September	8	NWS
2008	January	7	EE
2008	March/April	7	NWS
2009	March/April	297	WW
2009	June	67	WW
2010	February	13	PK
2010	June/July	124	WW

[a]Norma Wall Survey (NWS), Nebiha Shafi (NS), James Tagg (JT), Ed Elson (EE), Wendy Williams (WW), Paul Kotze (PK).

effective exposure time of 600 s. The resulting limiting magnitude is approximately 2 mag deeper than 2MASS (Riad 2010). This exposure time is long enough for the detection of fainter extragalactic objects while not so long that the field is saturated with the fainter old stellar population within our Galaxy. The field of view of the IRSF is well matched to the positional accuracy ($\lesssim$4 arcmin) of the H I sources (Donley et al. 2005); see also Fig. 9.

The observations for this pilot follow-up survey were started in 2006 and were continued through to 2010. Table 1 lists the progress of the observations and the observers who contributed to the survey. Some fields were observed as part of the Norma Wall Survey (NWS; Riad 2010). A total of seven weeks were allocated exclusively to this project; however, a significant amount of time (∼60 per cent) was lost due to bad weather and serious problems with the detector cooling system in 2010.

2.2 Target selection

Targets for the dedicated follow-up NIR observations were selected from a preliminary version of the HIZOA survey catalogue, containing ∼1100 sources. Our targets were further selected to lie within 6000 km s^{-1}. The reasons for this cut-off are as follows:

(i) this volume encompasses most of the large-scale structures in the nearby universe, including the Centaurus cluster, the Norma Wall/GA and the Hydra cluster (Radburn-Smith et al. 2006);

(ii) at this cut-off HIZOA is still sensitive to $M^*_{\rm H\,I}$ galaxies;

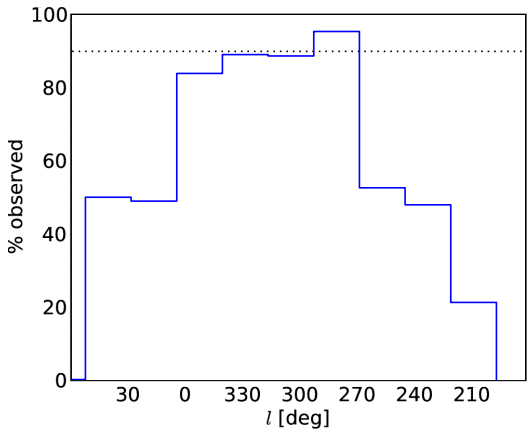

Figure 2. The percentage of galaxies observed out of the sample with $v < 6000$ km s^{-1} plotted in 20° bins of Galactic longitude. The relative incompleteness of the observations at both $l < 270°$ (Puppis/Hydra-Antlia filaments) and $l > 0°$ (Local Void) is evident, while the observations around the GA region are nearly complete.

(iii) an $M^*_{K_s} = -24.16$ mag galaxy (Kochanek et al. 2001) at 6000 km s^{-1} will have an apparent magnitude of 10.35 mag. Even with extinction of $A_{K_s} = 1$ mag ($A_B \approx 10$ mag), we should be able to detect galaxies up to 3.5 mag fainter than $M^*_{K_s}$ given a limiting magnitudes of 15.0 mag (for the NWS; Riad 2010);

(iv) the mass density within this volume and within the ZoA may have a significant effect on the motion of the Local Group (Kolatt et al. 1995; Loeb & Narayan 2008); and

(v) approximately 70 per cent of the HIZOA sources lie within this volume, giving us dense enough coverage to reveal a detailed flow field in the ZoA.

Fig. 1 shows the spatial distribution of all HIZOA candidate galaxies; the targets selected for NIR follow-up observations, i.e. those within 6000 km s^{-1}, are plotted with large blue points if they were observed and with red crosses if they were not observed during the allocated observing time. More distant HIZOA sources are plotted with small green points. The completeness fraction of the observations per longitude range is shown in Fig. 2. The relative incompleteness of the observations at both $l < 270°$ and $l > 0°$ is largely a result of the observing time lost due to poor weather and technical problems. The observations in the Norma region are nearly complete which is excellent for studying the flow fields around the

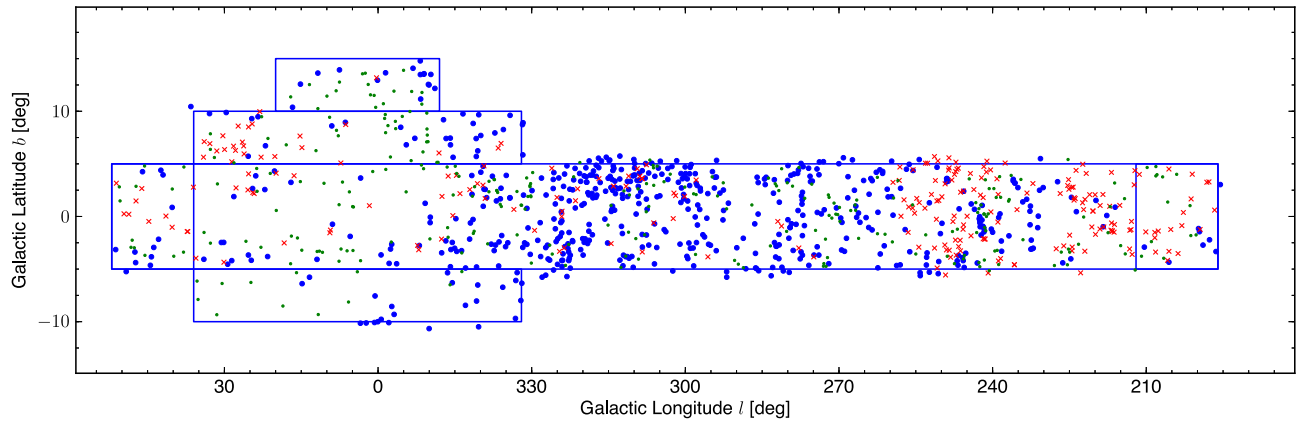

Figure 1. Observations completed within the allocated observing runs. The blue rectangles mark the HIZOA survey region. Of the 825 galaxies with $v \leq 6000$ km s^{-1} selected for observation, 578 (70 per cent) have been observed and are plotted with large blue circles. The remaining 247 are plotted with red crosses. The positions of the 286 HIZOA galaxies with $v > 6000$ km s^{-1} are indicated with small green points.

GA. Unfortunately, the completeness is ∼50 per cent or less around the Local Void and Puppis regions ($l < 0°$ and $l > 270°$, respectively). The impact of the low coverage for $l \lesssim 250°$ is somewhat compensated for by the better detection rate in the 2MASS extended source catalogue (2MASX; Jarrett et al. 2000) in this region due to the lower stellar density.

2.3 Data reduction and calibration

The data were reduced using the SIRIUS pipeline (Nakajima, private communication), which is a dedicated IRAF[2] package for the automated reduction of IRSF/SIRIUS images. The high-level steps that encompass the standard NIR image reduction include the following:

(i) dark current subtraction;
(ii) determination of master flat-fields and flat correction;
(iii) sky determination and subtraction; and
(iv) frame-to-frame offset determination and combination.

Sky frames are determined from a *self-sky* image produced by median combining the individual dithered frames without realigning them. Because detector artefacts remain fixed on the detector while astronomical sources move with the dither pattern, any features (e.g. stars) on scales less than the spacing between dithered frames will be removed, leaving only the sky structure. However, extended astronomical objects with scales larger than the field separation will leave a residual on the sky image.

The output images from the SIRIUS pipeline are astrometrically and photometrically calibrated against the 2MASS Point Source Catalogue (2MPSC; Strutskie 2006). The calibration is done with a combination of IRAF and PYTHON scripts developed by N. Matsunaga[3] and modified by Riad (2010). The astrometric calibration uses the method of Optimistic Pattern Matching (Tabur 2007) to match stars in the 2MPSC with point sources in each image. The astrometric solution is found using the IRAF task *ccmap*. We use J2000 coordinates.

The photometric calibration makes use of an IRAF script developed by Riad (2010) which matches point sources within 1.35 arcsec (3 pixels) in each image with sources in the 2MPSC. The instrumental magnitude, m^i_λ, is transformed to a standard magnitude by

$$m_\lambda = ZP^i_\lambda + m^i_\lambda,$$

where ZP_λ is the magnitude zero-point. The uncertainty in the zero-point of the standard star calibration was typically 0.06 mag in all three bands. The SIRIUS filters (Tokunaga, Simons & Vacca 2002) are slightly different from the 2MASS filters so a transformation is required between the two systems. This is applied only when comparing our results to 2MASS or in comparing to 2MTF. The 2MASS magnitudes (M') are first transformed to the SIRIUS system (M) via the following colour-dependent transformation equations (Nakajima, private communication):

$$J = J' + (-0.045 \pm 0.008)(J - H)' - (0.001 \pm 0.008)$$

$$H = H' + (0.027 \pm 0.007)(J - H)' - (0.009 \pm 0.008)$$

$$K_s = K'_s + (0.015 \pm 0.008)(J - K_s)' - (0.001 \pm 0.008)$$

[2] Image Reduction and Analysis Facility (IRAF) is distributed by the National Optical Astronomy Observatory (NOAO), which is operated by the Association of Universities for Research in Astronomy, Inc., under cooperative agreement with the National Science Foundation.
[3] Institute of Astronomy, School of Science, University of Tokyo.

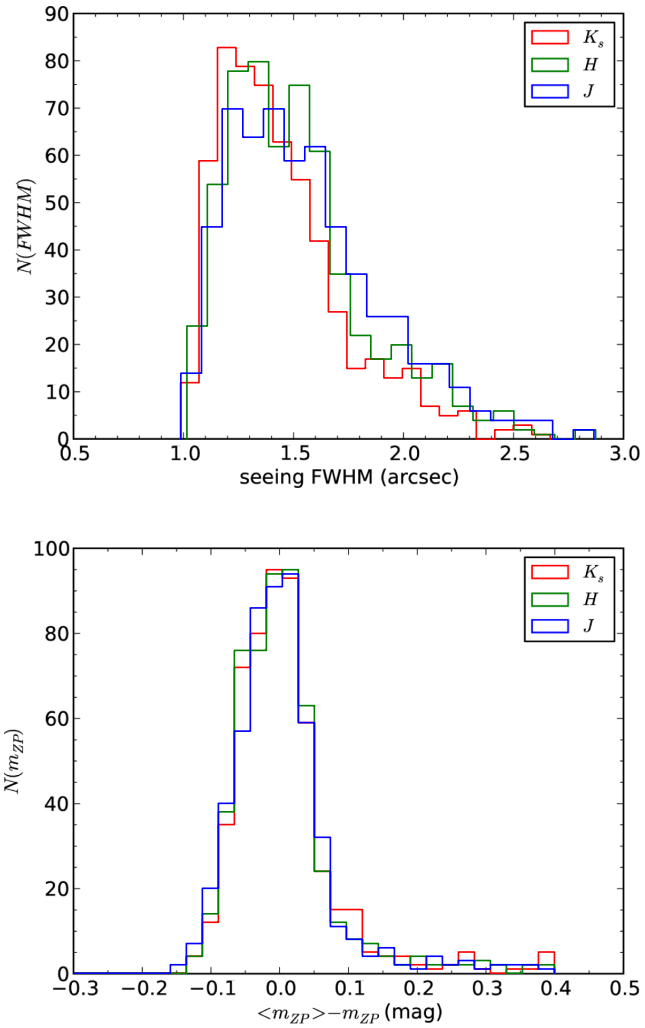

Figure 3. Histograms of image FWHM as a measure of the seeing and image magnitude zero-points as a measure of the image quality.

Table 2. Mean magnitude zero-points and average seeing for all 578 images.

	⟨ZP⟩ (mag)	σ (mag)	Seeing (arcsec)	σ (arcsec)
J	20.84	0.06	1.49	0.35
H	21.02	0.06	1.47	0.33
K_s	20.24	0.06	1.39	0.30

which are valid over a wide range in colour $0.0 \leq (J - H) \leq 3.9$, $0.0 \leq (H - K_s) \leq 2.8$ and $0.0 \leq (J - K_s) \leq 4.9$.

Two measures of the photometric conditions are determined for each field: the seeing, or full width at half-maximum (FWHM) of stars in the field, and the magnitude zero-point. Fig. 3 shows the distribution of seeing values and magnitude zero-points for all of the final 578 images. 65 per cent of the images were observed with K_s-band seeing of <1.5 arcsec and 85 per cent with <1.75 arcsec. The median zero-points are consistent with values previously determined by Riad (2010) and Cluver et al. (2008). The medians and standard deviations of both the magnitude zero-points and seeing values in all three bands are given in Table 2.

3 SURFACE PHOTOMETRY

3.1 Galaxy identification

Possible NIR counterparts to the H I sources were identified in the respective NIR images by a visual search of the false three-colour (RGB) images generated from the K_s, H and J bands where the K_s image is mapped to the red channel, the H image to green and the J image to blue. Their different colour and extended nature allow galaxies to be readily identified by eye. A PYTHON script, which uses the PYDS9[4] interface with SAOImage DS9,[5] was used to interactively and systematically search the 7.7 arcmin × 7.7 arcmin images for possible counterparts to the H I sources. The likelihood of a counterpart was assessed based on the NIR images and the H I spectral features. For example, an obvious elliptical galaxy would be excluded in preference of an edge-on spiral galaxy if the H I profile showed a clear double-horn structure. This is described further in Section 4.1.

3.2 Star subtraction

The increase in stellar density near the Galactic plane results in heavy contamination by foreground stars. Star subtraction by fitting the point spread function (PSF) was employed to remove the flux contribution of the foreground stars from the galaxy flux. This is implemented in two steps: the PSF is first determined for the field, which may be variable across the field. Secondly, the fitted PSF is used to remove stars in the neighbourhood of each detected galaxy. The automated PSF fitting routine for the NWS (Nagayama, private communication) was modified to improve the subtraction of stars on edge-on discs and to prevent the removal of sub-structure within the discs of face-on spirals. The method of star subtraction is based on the KILLALL routine (Buta & McCall 1999). The steps, implemented in PYRAF, are as follows.

(i) The sky background and rms, σ, in the image is determined using IMSTATISTICS with 30 iterations with 3σ clipping.

(ii) The galaxy is modelled using ELLIPSE and BMODEL. This model is subtracted from the image resulting in the galaxy-subtracted image. Structures on the galaxy, in particular spiral arms, may not be fully modelled and may result in residuals in the galaxy-subtracted image.

(iii) The bright stars (above 3.5σ of the background) in the galaxy-subtracted image are detected and removed with SExtractor (Bertin & Arnouts 1996). The DAOPHOT tasks PHOT and ALLSTAR are used to measure the PSF photometry of these sources and then to remove them from the galaxy-subtracted image.

(iv) The faint stars (above 1.8σ) are then detected and removed from the galaxy-subtracted image. Within the radius of the galaxy only stars that are also detected by DAOFIND with a threshold of 2σ are included in the list. This prevents the misidentification of residuals of structures as stars. Again PSF photometry is done with PHOT and the stars are removed from the galaxy-subtracted image using ALLSTAR.

(v) The two ALLSTAR output files for the bright and faint stars are concatenated, and used in SUBSTAR to remove these stars from the original image.

(vi) Any residuals as a result of the imperfect fit of the PSF to every star in the image are found and removed.

Steps (ii) to (vi) are iterated four times. Each iteration improves the galaxy model because the subtraction of stars on the galaxy gets more accurate. This results in improved photometry of stars on the galaxy and therefore increasingly reliable subtraction.

Fig. 4 shows some examples of the results of the star-subtraction routine. It displays qualitatively that the star subtraction performs well. The removal of stars in this manner has been shown to have a minimal effect on the uncertainty in the galaxy photometry. In simulations of subtracting an artificially added star field from galaxies, Nagayama et al. (2004) found that the measured K_{s20} magnitudes (the magnitude within the radius to the $K_s = 20$ mag arcsec^{-2} isophote) were on average 0.04 mag fainter with a standard deviation of 0.20 mag.

3.3 Astrometric parameters

3.3.1 Source positions

The position is measured using the intensity-weighted centroid of the $J + H + K_s$ 'super' co-add image. This position should be more precise as it measures the centroid from higher signal-to-noise (S/N) data. The catalogue identifiers are `RA, Dec.` for the J2000 equatorial coordinates in degrees and `l, b` for the Galactic coordinates in degrees.

3.3.2 Ellipse fitting and object orientation

Ellipses were fitted to each galaxy image using the IRAF task ELLIPSE. The central coordinates, (X, Y), are fixed while the position angle (ϕ, measured counter-clockwise from the x-axis) and ellipticity ($\epsilon = 1 - b/a$) are fitted at intervals in the semi-major axis. ELLIPSE returns a table containing, amongst others, the intensity in counts enclosed within the ellipse, the position angle, the ellipticity and their errors at each semi-major axis step. The ellipticity and position angle characteristic of the galaxy are determined to be the average value in the outer part of the disc, between the 1σ and 2σ isophotes, where σ is the sky rms. Both the ellipticity and the position angle are usually stable in the outer disc. The ellipse parameters are determined individually in all three bands.

The ellipticities are identified in the catalogue as ⟨`band`⟩`_ell` where ⟨`band`⟩ is one of `j`, `h` or `k` for the J, H or K_s bands, respectively. The 1σ errors are identified by ⟨`band`⟩`_ell_sig`. The position angles and errors (in J2000 coordinates, measured east of north) are listed in the catalogue as ⟨`band`⟩`_phi` and ⟨`band`⟩`_phi_sig`, respectively.

3.4 Self-sky correction for large galaxies

The nature of the *self-sky* measurement means that galaxies larger than the dither radius overlap in the individual dithered frames. The final sky frame therefore contains an extended residual, typically of a few counts per pixel above the average sky value, in the region of the galaxy. The result is that too much sky is subtracted from the region around the galaxy causing the measured fluxes to be lower. This is clearly evident in the intensity profile of the galaxy as a dip in flux around the outer edges below the median sky level. The residual is such that it is largest in the centre of the galaxy, decreasing towards the outer parts. However, it cannot be measured directly at the centre of the galaxy. We therefore measure the shape of the

[4] http://hea-www.harvard.edu/saord/pyds9/

[5] This research has made use of SAOImage DS9, developed by Smithsonian Astrophysical Observatory.

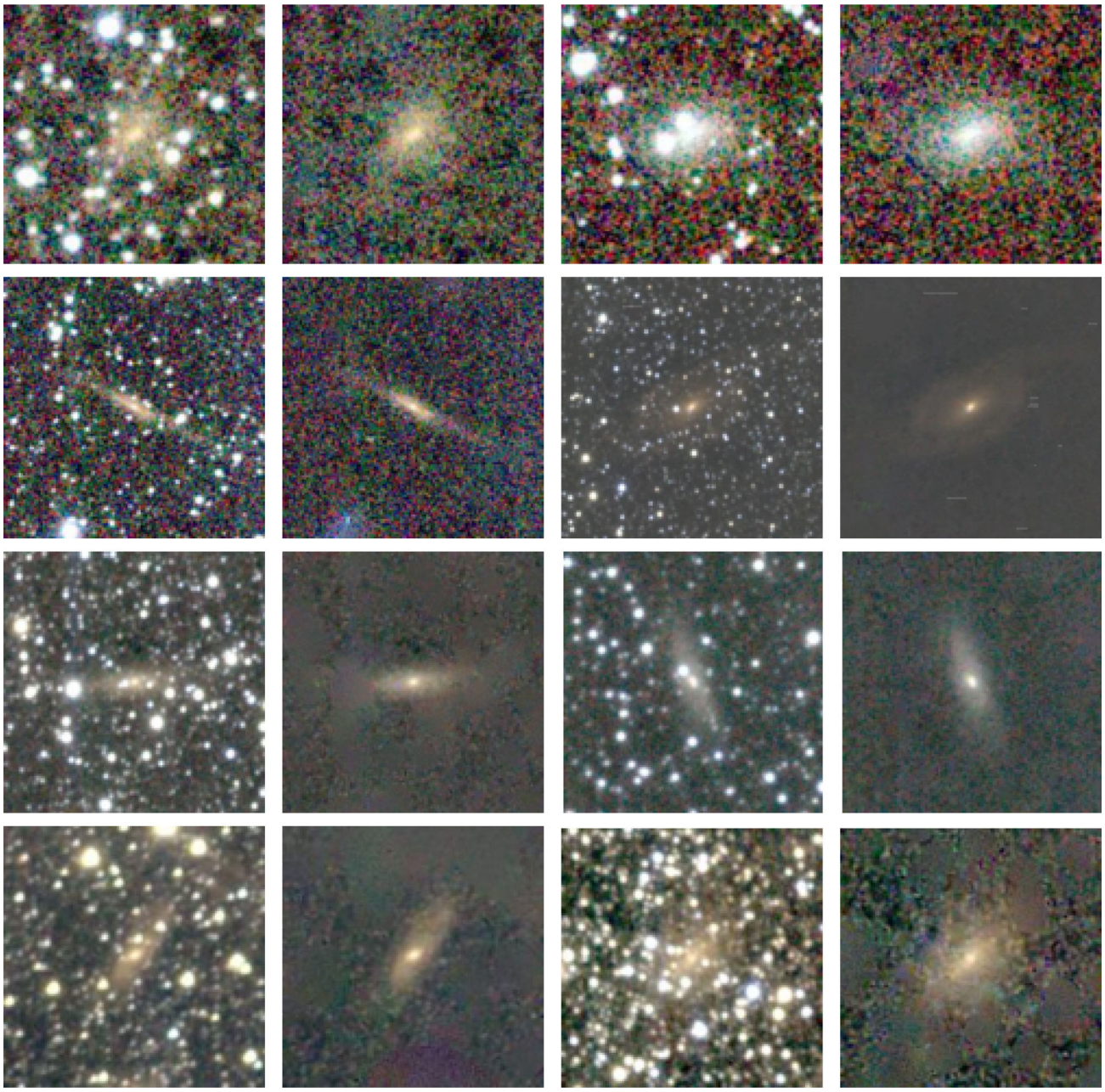

Figure 4. Examples of starry and star-subtracted postage stamp images. The colours of the galaxies are representative of the observed NIR colours.

recovery of the dip in the outer parts to the sky level and extrapolate to the centre. This is done by fitting a linear function to the intensity profile between the minimum intensity and the asymptotic sky value and adding this to the intensity profile. A linear function was chosen as it is the simplest function that describes the shape of the dip. It provides a first-order correction while introducing as little error as possible from higher order terms. The size of the correction at the centre of the galaxy can be up to 5–10 counts pixel^{-1} for large galaxies with bright extended cores. However, this affects only a small number of galaxies, ∼20.

A correction for this effect is made for galaxies which have both semi-major and semi-minor axes that are larger than the dither radius. As an example for one galaxy (J0748−26B), Fig. 5 shows the *H*-band intensity profile. The red profile is uncorrected. The blue line shows the fit that has been made from the minimum in the profile to the outer edges. The fit region is demarcated by two vertical lines. The horizontal line shows the measured median sky value. The blue profile shows the corrected intensity profile.

3.5 Photometric parameters

3.5.1 Fixed aperture magnitudes

The simplest photometric measurement is for fixed circular apertures. Magnitudes are measured using a PYTHON routine for apertures of 3, 5, 7, 10 and 15 arcsec. The magnitudes and their errors are identified in the catalogue as ⟨band⟩_m⟨c⟩, ⟨band⟩_msig⟨c⟩, where

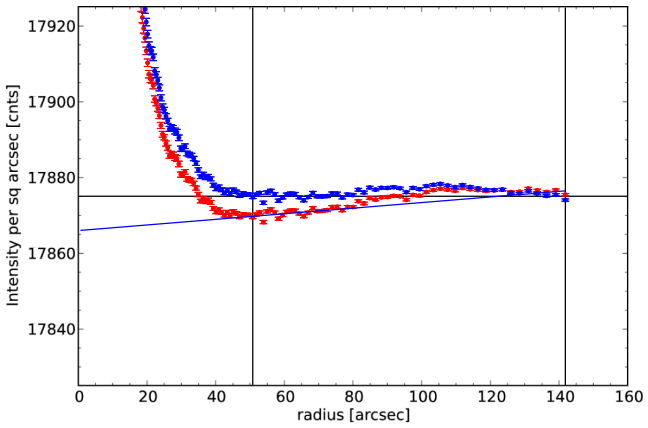

Figure 5. Example intensity profile with self-sky correction. The red profile shows the intensity profile before the correction. A linear function is fitted to the outer part of the profile from the minimum (blue line) to the outer edge where the sky level is reached. The limits of the fit are shown with solid vertical lines. The horizontal line shows the measured median sky level in the image. The blue profile shows the corrected profile.

⟨band⟩ is the band in which the magnitude is measured and ⟨c⟩ is the radius, in arcsec, of the aperture.

3.5.2 *Radial surface brightness profiles*

The one-dimensional radial surface brightness profile (SBP) is measured with ELLIPSE by holding the centre, position angle and ellipticity fixed. The SBPs of each galaxy were fitted with a double Sérsic function,

$$\mu(a) = \mu_0 + 1.086\left(\frac{a}{r_h}\right)^n + \mu_{02} + 1.086\left(\frac{a}{r_{h_2}}\right)^{n_2},$$

or in terms of intensities,

$$I(a) = I_0 \exp\left(\frac{a}{r_h}\right)^n + I_{02}\exp\left(\frac{a}{r_{h_2}}\right)^{n_2}.$$

The double Sérsic function is the most general profile that allows for the simultaneous fitting of both an inner bulge (usually following a de Vaucouleurs profile with $n = 4$) and an outer disc profile (exponential with $n_2 = 1$).

A plot of the SBP in each band is produced which shows the measured SBP, the fitted SBP, the residuals, the fitted parameters, a grey-scale image and the ellipse parameters. Examples of such SBP plots for J0748−26B are shown in Fig. 6.

3.5.3 *Isophotal magnitudes*

Isophotal elliptical aperture photometry is performed in each band, using the ELLIPSE task. The isophotal radius, r_μ, is the radius of the isophote at surface brightness μ. The isophotal magnitude, m_μ, is defined as the integrated magnitude within that radius. In each band, the $\mu = 20$, 21 and 22 mag arcsec^{-2} isophotal radii and magnitudes are calculated. The SBP is used to determine the radius at which a given surface brightness is reached. The catalogue names are `r_`⟨band⟩`20e`, ⟨band⟩`_m_`⟨band⟩`20e` and ⟨band⟩`_msig_`⟨band⟩`20e` for the 20 mag arcsec^{-2} isophotal radius, magnitude and error, respectively, in the given band. The fiducial isophotal parameters are `r_`⟨band⟩`20fe`, ⟨band⟩`_m_`⟨fband⟩`20fe` and ⟨band⟩`_msig_`⟨fband⟩`20fe` for the 20 mag arcsec^{-2} isophotal radius, magnitude and error, respectively, in the given band where the fiducial band is `fband`.

3.5.4 *Total magnitudes*

Following a similar analysis to Kirby et al. (2008), extrapolation of the analytic double Sérsic function allows for an accurate estimate of

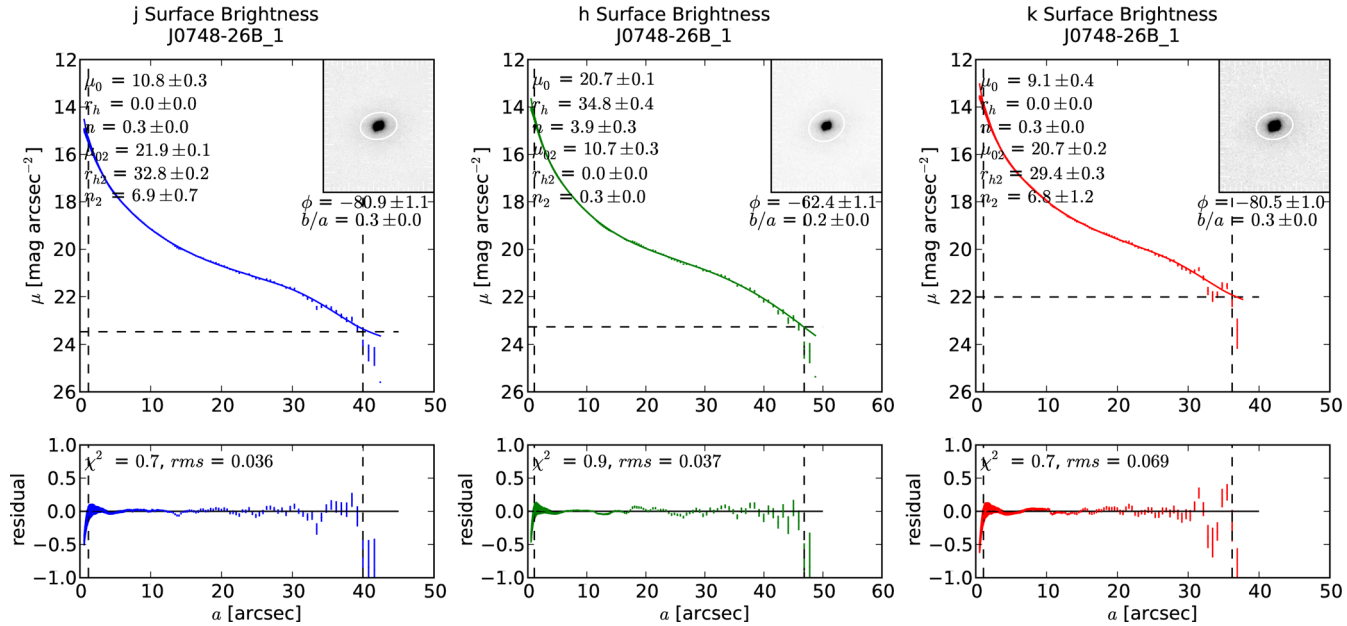

Figure 6. Example of radial SBP plots in the J (left), H (centre) and K_s (right) bands for galaxy J0748−26B. The best-fitting double Sérsic function to the outer part of the profile is shown as a solid line together with the residuals in the bottom panel. The rms of the fit, in mag arcsec^{-2}, is given in the top-left corner of the bottom panel. The inset panel shows a grey-scale image of the galaxy, with the characteristic ellipse in white. The parameters of the ellipse are given below the inset and the radius of the ellipse is determined to be the 1σ isophote, which is marked on the SBP by the horizontal and vertical dashed lines.

the flux that remains undetected below the sky noise. The integrated flux between a given outer radius, $r_{\rm out}$, and $r = \infty$ is

$$\Delta m = -2.5 \log \left(\frac{I_{\rm missing}}{I_{\rm total}} \right),$$

where

$$I_{\rm missing} = \int_0^{a_{\rm tot}} 2\pi(1-\epsilon) I(a) a \, {\rm d}a$$

$$= \int_0^{a_{\rm tot}} 2\pi(1-\epsilon) \left[I_0 \exp \left(\frac{a}{r_h} \right)^n + I_{02} \exp \left(\frac{a}{r_{h_2}} \right)^{n_2} \right] a \, {\rm d}a$$

$$= 2\pi(1-\epsilon) \left\{ \frac{I_0 r_h^2}{n} \Gamma \left[\frac{2}{n}, \left(\frac{r_{\rm tot}}{r_h} \right)^n \right] + \frac{I_{02} r_{h_2}^2}{n_2} \Gamma \left[\frac{2}{n_2}, \left(\frac{r_{\rm tot}}{r_{h_2}} \right)^{n_2} \right] \right\}$$

and

$$I_{\rm total} = \int_0^{\infty} 2\pi(1-\epsilon) I(a) a \, {\rm d}a$$

$$= \int_0^{\infty} 2\pi(1-\epsilon) \left[I_0 \exp \left(\frac{a}{r_h} \right)^n + I_{02} \exp \left(\frac{a}{r_{h_2}} \right)^{n_2} \right] a \, {\rm d}a$$

$$= 2\pi(1-\epsilon) \left\{ \frac{I_0 r_h^2}{n} \Gamma \left[\frac{2}{n} \right] + \frac{I_{02} r_{h_2}^2}{n_2} \Gamma \left[\frac{2}{n_2} \right] \right\}.$$

$\Gamma[\alpha, x]$ is the incomplete gamma function and $a_{\rm tot}$ was taken to be the radius at which the surface brightness drops to 1σ. The observed total magnitude, $m_{\rm obs}$, is the magnitude enclosed within this aperture. The total magnitude is then determined to be

$$m_{\rm tot} = m_{\rm obs} - \Delta m.$$

The catalogue parameters are ⟨band⟩_m_ext for the extrapolated total magnitude, ⟨band⟩_msig_ext for the error and ⟨band⟩_dm_ext for the difference between total magnitude and the measured outer magnitude.

3.5.5 Photometric errors

The fundamental limits to the photometry depend on the accuracy of the background determination, the S/N within the aperture and the zero-point calibration. The error, σ_F, on a flux within a given aperture, F, is the quadrature sum of the Poissonian source noise and the error in the sky background:

$$\sigma_F = \sqrt{F + N\sigma_{\rm rms}^2},$$

where N is the number of pixels in the aperture and $\sigma_{\rm rms}$ is the sky background.

The ellipse fitting procedures will introduce additional errors. However, these are neglected here as they are expected to be less significant than the errors already mentioned.

3.6 Galaxy types

Based on visual inspection of the NIR images, we made an estimate of the morphological type of each galaxy: galaxies with no obvious bulge were classed as late-type (Hubble T-type 5), those with a clear bulge were classed as early-type spirals (T-type 1) and those with some evidence of a bulge as intermediate (T-type 3). Consideration was made for the effects of extinction, which can lead to the outer parts of the galaxies disappearing and the galaxy appearing more 'bulge'-like; however, we do note that this is an estimate only. Approximately 15 per cent were classed as early-type spirals, 70 per cent were classed as intermediate-type spirals and 15 per cent were classed as late-type spirals.

3.7 Catalogue

The 40 brightest galaxies in the catalogue are presented, as an example, in Table 3. The columns are as follows: column 1 – unique identifier [ZOAhhmmss.sss±ddmmss.ss] from the co-add centroid (see Section 3.3.1); column 2 – H I catalogue name [Jhhmm±dd]; column 3 – counterpart number (can be greater than 1 where more than one possible counterpart was identified in the IRSF field of view) followed by an ⋆ if it is confirmed; columns 4 and 5 – Galactic coordinates [deg]; columns 6 – J-band ellipticity ($\epsilon = 1 - b/a$) and error; column 7 – J-band position angle (east of north) and error [deg]; column 8 – K_{s20} fiducial isophotal radius [arcsec]; columns 9–11 – J-, H- and K_s-band K_{s20} fiducial isophotal magnitude and error [mag]; columns 12–14 – J-, H- and K_s-band extrapolated total magnitude [mag]; column 15 – Galactic reddening along the line of sight (Schlegel, Finkbeiner & Davis 1998) [mag]; and column 16 – stellar density for stars brighter than 14 mag in K_s detected with the IRSF. All magnitudes are given as IRSF/SIRIUS magnitudes, not transformed to 2MASS. The catalogue in its entirety, with all measured parameters, is available in the electronic supplement.

3.8 Comparison with 2MASX

To evaluate the consistency of our photometry, we compare the astrometric and photometric parameters of a sample of our galaxies that appear in the 2MASX catalogue. 2MASX positional errors are typically around 0.5 arcsec. Sources are assumed to be identical in the two catalogues if they are separated by less than 1.5 arcsec. This small correlation radius is taken because the SIRIUS images have been astrometrically calibrated against the 2MASX. Moreover, in many cases, the 2MASS coordinates are offset from the IRSF coordinates because the source is centred on a nearby foreground star which has not been removed. Only sources with reliable IRSF photometry are compared, i.e. galaxies near the edge of the field are excluded; 102 galaxies are included in the comparison.

In Fig. 7, we show a comparison of the IRSF/SIRIUS and 2MASX positions. We find that the offset of ΔRA of $-0\farcs02$ is small and consistent with zero, with a dispersion of 0.61 arcsec, and ΔDec. of $-0\farcs02$ with a dispersion of 0.54 arcsec. Riad (2010) finds similar values of ΔRA $= -0\farcs01$ with a dispersion of 0.42 arcsec, and ΔDec. $= 0\farcs11$ with a dispersion of 0.39 arcsec. This is consistent with the expected combined error of 2MASX and IRSF/SIRIUS of $\sigma = 0.44$ arcsec (Riad 2010).

Next, we compare the IRSF photometric parameters with the 2MASX values. The comparison is made for both the 5 arcsec aperture magnitudes and the $K_s = 20$ mag arcsec^{-2} fiducial isophotal magnitudes in all three bands (see Fig. 8). The metric used is

$$\Delta m = m(\text{2MASS}) - m(\text{IRSF});$$

thus, a positive quantity means that the 2MASS magnitude is fainter than the IRSF. All IRSF/SIRIUS magnitudes are transformed to the 2MASS standard via the transformation given by Nakajima (private communicationBsemi see Section 2.3). The mean offsets and dispersions are summarized in Table 4; these are smaller for the 5 arcsec aperture than the isophotal magnitudes. This is expected given the smaller apertures used, although they may be more affected by the

Table 3. Selected measured galaxy parameters for the 40 brightest K_{s20} magnitude galaxies in the catalogue. The catalogue in its entirety, with all measured parameters, is available in the electronic supplement.

Designation	H name	#	l (deg)	b (deg)	ϵ_J	ϕ_J (deg)	r_{k20fe} (arcsec)	J_{k20fe} (mag)	H_{k20fe} (mag)	K_{sk20fe} (mag)	$J_{\rm tot}$ (mag)	$H_{\rm tot}$ (mag)	$K_{s,\rm tot}$ (mag)	$E(B-V)$ (mag)	SD
ZOA141309.873−652020.76	J1413−65	1⋆	311.326	−3.808	0.44	37.6	87.05	7.50 ± 0.02	6.49 ± 0.02	6.09 ± 0.02	7.08 ± 0.12	6.39 ± 0.02	6.17 ± 0.03	1.47	4.37
ZOA151434.147−525921.52	J1514−53	1⋆	323.594	4.043	0.76	−16.9	136.09	8.86 ± 0.02	7.91 ± 0.02	7.42 ± 0.02	8.95 ± 0.03	7.83 ± 0.03	7.34 ± 0.02	0.99	4.30
ZOA085728.494−391605.86	J0857−39	1⋆	261.500	4.100	0.09	27.6	44.85	9.19 ± 0.02	8.32 ± 0.02	7.97 ± 0.02	9.20 ± 0.02	8.09 ± 0.06	8.02 ± 0.03	0.72	3.61
ZOA150928.962−523320.67	J1509−52	1⋆	323.155	4.810	0.79	45.3	98.73	9.24 ± 0.02	8.38 ± 0.02	7.97 ± 0.02	8.77 ± 0.14	8.35 ± 0.03	7.86 ± 0.03	0.77	4.09
ZOA122238.290−583657.66	J1222−58	1⋆	299.180	4.046	0.69	−27.0	60.30	9.71 ± 0.02	8.92 ± 0.02	8.60 ± 0.02	9.68 ± 0.02	8.57 ± 0.10	8.61 ± 0.02	0.58	4.12
ZOA145709.815−542331.46	J1457−54	1⋆	320.654	4.096	0.50	51.6	53.81	10.05 ± 0.02	9.14 ± 0.02	8.69 ± 0.02	9.83 ± 0.08	8.94 ± 0.06	8.59 ± 0.02	0.85	4.21
ZOA094916.505−475511.27	J0949−47A	1	274.257	4.549	0.06	28.9	38.65	9.67 ± 0.02	8.98 ± 0.02	8.69 ± 0.02	9.59 ± 0.04	8.85 ± 0.04	8.71 ± 0.03	0.35	3.80
ZOA114606.371−562326.95	J1145−56	1⋆	293.937	5.336	0.27	−48.5	54.68	9.99 ± 0.02	9.26 ± 0.02	8.82 ± 0.02	9.41 ± 0.20	8.45 ± 0.24	8.41 ± 0.11	0.39	3.84
ZOA135138.534−583515.22	J1351−58	1⋆	310.724	3.370	0.52	32.3	47.27	10.23 ± 0.02	9.31 ± 0.02	8.87 ± 0.02	10.18 ± 0.03	9.27 ± 0.02	8.55 ± 0.09	0.97	4.29
ZOA080610.996−273140.54	J0805−27	1	245.709	2.414	0.05	−13.3	52.34	10.39 ± 0.02	9.38 ± 0.02	8.89 ± 0.02	10.45 ± 0.03	9.37 ± 0.02	8.86 ± 0.02	0.42	3.78
ZOA074752.048−184453.18	J0747−18	1⋆	236.009	3.374	0.82	−82.1	84.90	10.06 ± 0.02	9.31 ± 0.02	8.91 ± 0.02	9.83 ± 0.06	8.80 ± 0.14	8.64 ± 0.08	0.38	3.55
ZOA143158.829−552758.82	J1431−55	1⋆	316.912	4.653	0.05	82.6	34.39	10.32 ± 0.02	9.46 ± 0.02	9.05 ± 0.02	9.74 ± 0.19	8.60 ± 0.27	8.56 ± 0.15	0.85	4.09
ZOA163211.878−280530.82	J1632−28	1⋆	351.084	13.502	0.72	−52.8	81.48	10.28 ± 0.02	9.45 ± 0.02	9.10 ± 0.02	10.13 ± 0.06	9.28 ± 0.03	8.97 ± 0.02	0.61	3.54
ZOA141036.181−653457.76	J1410−65	1⋆	310.997	−3.958	0.52	−87.4	46.18	10.35 ± 0.02	9.48 ± 0.02	9.14 ± 0.02	10.31 ± 0.03	9.39 ± 0.02	8.72 ± 0.12	0.60	4.32
ZOA074843.902−261446.34	J0748−26	1⋆	242.586	−0.239	0.30	−27.9	31.93	10.71 ± 0.02	9.78 ± 0.02	9.25 ± 0.02	9.82 ± 0.29	9.70 ± 0.03	8.97 ± 0.08	0.72	3.84
ZOA091645.231−542124.17	J0916−54B	2	274.871	−3.630	0.67	56.3	30.08	9.61 ± 0.02	9.27 ± 0.02	9.28 ± 0.02	8.84 ± 0.25	8.70 ± 0.17	8.83 ± 0.13	0.94	3.99
ZOA083439.531−400855.61	J0834−40	1⋆	259.448	0.122	0.22	20.8	34.38	10.02 ± 0.02	9.52 ± 0.02	9.30 ± 0.02	9.41 ± 0.21	9.11 ± 0.12	8.55 ± 0.22	2.12	3.84
ZOA132723.827−572922.23	J1327−57	1⋆	307.768	5.044	0.74	1.6	46.73	10.86 ± 0.02	9.82 ± 0.02	9.30 ± 0.02	11.03 ± 0.02	9.76 ± 0.02	9.10 ± 0.05	0.81	3.98
ZOA085838.816−423157.53	J0858−42	1⋆	264.125	2.141	0.44	63.0	42.93	12.14 ± 0.02	10.09 ± 0.02	9.35 ± 0.02	12.23 ± 0.04	9.75 ± 0.08	9.20 ± 0.04	3.99	3.73
ZOA094952.868−563235.55	J0949−56	1⋆	279.808	−2.054	0.24	−67.6	45.57	11.43 ± 0.02	10.29 ± 0.02	9.58 ± 0.02	11.03 ± 0.23	9.78 ± 0.12	9.01 ± 0.14	2.10	4.16
ZOA141933.720−580850.19	J1419−58	1⋆	314.363	2.755	0.59	19.7	52.89	11.00 ± 0.02	10.14 ± 0.02	9.59 ± 0.02	10.80 ± 0.08	10.02 ± 0.03	9.41 ± 0.03	1.52	4.36
ZOA163140.118−280606.66	J1631−28	1⋆	350.997	13.584	0.27	69.5	35.29	10.83 ± 0.02	10.07 ± 0.02	9.59 ± 0.02	10.70 ± 0.05	9.40 ± 0.20	9.45 ± 0.03	0.63	3.60
ZOA090033.130−392627.15	J0900−39	1⋆	262.020	4.438	0.40	−53.9	37.84	10.79 ± 0.02	10.15 ± 0.02	9.67 ± 0.02	10.70 ± 0.03	10.18 ± 0.03	9.63 ± 0.02	0.67	3.61
ZOA161319.695−562349.17	J1613−56	1⋆	328.261	−3.802	0.35	−70.7	40.49	10.93 ± 0.02	10.69 ± 0.02	9.68 ± 0.02	10.58 ± 0.13	9.82 ± 0.31	9.29 ± 0.09	0.54	4.43
ZOA162101.624−360831.49	J1621−36	1⋆	343.413	9.765	0.55	54.2	38.44	10.84 ± 0.02	10.05 ± 0.02	9.71 ± 0.02	10.51 ± 0.11	9.83 ± 0.05	9.41 ± 0.08	0.71	3.79
ZOA074252.007−315959.79	J0742−31	1⋆	246.932	−4.226	0.52	31.9	26.61	11.15 ± 0.02	10.38 ± 0.02	9.71 ± 0.02	11.08 ± 0.04	10.41 ± 0.02	9.33 ± 0.11	0.83	3.76
ZOA101212.032−623159.40	J1012−62	1⋆	285.685	−5.121	0.62	41.4	39.84	10.84 ± 0.02	10.08 ± 0.02	9.71 ± 0.02	10.77 ± 0.04	9.73 ± 0.09	9.49 ± 0.05	0.29	4.04
ZOA114948.692−640006.93	J1149−64	1	296.241	−1.934	0.57	−63.4	42.66	11.73 ± 0.02	10.42 ± 0.02	9.73 ± 0.02	11.08 ± 0.29	9.84 ± 0.16	9.13 ± 0.16	2.44	4.38
ZOA141710.099−553238.77	J1416−55	1⋆	314.915	5.320	0.86	14.5	68.61	11.23 ± 0.02	10.10 ± 0.02	9.73 ± 0.02	11.16 ± 0.03	9.39 ± 0.17	9.21 ± 0.15	0.62	3.98
ZOA074141.201−223112.25	J0741−22	1⋆	238.558	0.239	0.80	−20.1	48.26	11.31 ± 0.02	10.24 ± 0.02	9.74 ± 0.02	11.03 ± 0.07	9.30 ± 0.25	9.68 ± 0.02	0.66	3.74
ZOA161710.749−581844.59	J1617−58	1⋆	327.304	−5.542	0.53	79.0	33.09	10.82 ± 0.02	10.04 ± 0.02	9.75 ± 0.02	10.68 ± 0.04	9.63 ± 0.08	9.65 ± 0.03	0.30	4.16
ZOA073008.083−220105.84	J0730−22	1⋆	236.817	−1.851	0.77	22.5	104.61	11.51 ± 0.02	10.04 ± 0.02	9.78 ± 0.02	10.71 ± 0.51	9.25 ± 0.11	9.20 ± 0.07	1.81	3.69
ZOA075220.625−250840.47	J0752−25A	1⋆	242.052	1.022	0.56	35.4	33.38	10.92 ± 0.02	10.17 ± 0.02	9.79 ± 0.02	10.78 ± 0.05	10.02 ± 0.03	9.03 ± 0.23	0.38	3.68
ZOA175453.601−342057.64	J1755−34	1⋆	356.354	−4.464	0.37	−15.7	33.99	11.04 ± 0.02	10.35 ± 0.02	9.83 ± 0.02	10.77 ± 0.16	9.73 ± 0.19	9.28 ± 0.16	0.70	4.86
ZOA182226.663−354035.70	J1822−35	1⋆	357.859	−10.062	0.65	87.5	37.90	10.98 ± 0.02	10.14 ± 0.02	9.84 ± 0.02	10.76 ± 0.07	10.01 ± 0.04	9.09 ± 0.21	0.14	4.11
ZOA141604.868−651502.53	J1416−65	1⋆	311.644	−3.821	0.48	69.7	36.60	11.23 ± 0.02	10.32 ± 0.02	9.90 ± 0.02	10.48 ± 0.26	10.10 ± 0.04	9.38 ± 0.14	0.77	4.31
ZOA105345.693−625013.17	J1053−62	1⋆	289.956	−2.968	0.67	−20.5	65.48	11.60 ± 0.02	10.68 ± 0.02	9.90 ± 0.02	11.37 ± 0.16	10.57 ± 0.05	9.71 ± 0.02	0.83	4.23
ZOA133732.784−585414.06	J1337−58B	2	308.867	3.436	0.28	−16.5	33.07	11.33 ± 0.02	10.31 ± 0.02	9.92 ± 0.02	10.93 ± 0.13	9.93 ± 0.06	9.70 ± 0.05	1.09	4.30
ZOA191724.683+074909.02	J1917+07	1⋆	42.853	−2.159	0.30	69.8	34.25	11.44 ± 0.02	10.40 ± 0.02	9.94 ± 0.02	11.18 ± 0.10	10.14 ± 0.06	9.90 ± 0.02	1.94	4.51
ZOA143927.759−552503.43	J1439−55	1⋆	317.910	4.281	0.22	44.9	30.55	11.17 ± 0.02	10.41 ± 0.02	9.97 ± 0.02	10.83 ± 0.11	9.68 ± 0.21	9.10 ± 0.26	0.64	4.11

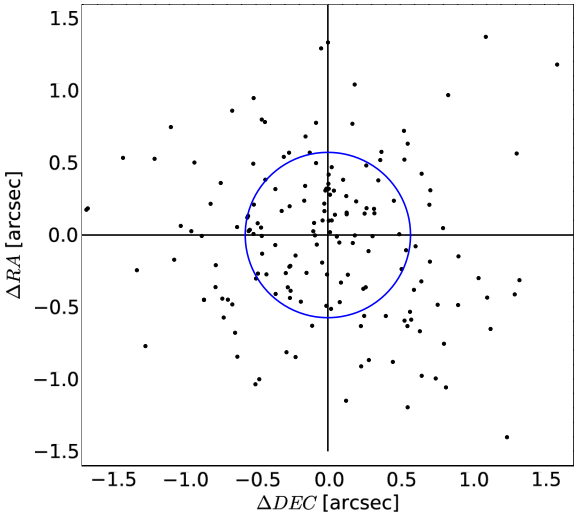

Figure 7. Comparison of the IRSF and 2MASX positions. The ellipse shows the 1σ dispersion in the positions.

different methods used for determining the position.[6] Note that seeing corrections are deemed negligible given the excellent observing conditions.

On average, we find that the IRSF isophotal magnitudes are fainter than the 2MASX magnitudes. This is not surprising: the higher resolution of IRSF/SIRIUS improves the detection and subtraction of faint stars within the isophotal radius. The dispersion is approximately two times that obtained by Riad (2010) and Cluver et al. (2008), who find a dispersion of 0.095 and 0.07 mag, respectively, in K_s. Skelton (2007) finds a higher dispersion of 0.19, more consistent with our values. However, our larger dispersion may originate from the fact that our sample is composed mostly of spiral galaxies, many of which have extended faint discs, whereas Riad's sample contains many more elliptical galaxies. Moreover, our sample does cover a very wide range of Galactic longitude and latitude. Note also that the $K_s = 20$ mag fiducial isophotal magnitudes are measured in differently determined apertures.

4 DISCUSSION

4.1 Detection rates

The NIR catalogue contains all galaxies identified as possible NIR counterparts to the H I sources, including some additional NIR galaxies where the counterpart was uncertain. Both the H I spectra and NIR images were used to aid in the counterpart identification. For instance, a galaxy with a clear double-horn profile was identified as an edge-on NIR galaxy and one with a flat-top profile was identified as a face-on galaxy. We also took the foreground extinction into account: e.g. if the H I profile was suggestive of a late-type spiral but in a very high extinction region we allowed the galaxies to be more elliptical and bulgy in appearance because most of the low surface brightness disc will have been lost in the extinction. In the cases of positive identification of the NIR counterpart, usually only the presence of a strong double-horn profile and clearly inclined galaxy allowed for confirmation of the counterpart. In the 578 fields that were observed, a total of 557 galaxies were identified in 421 fields. 317 fields had a single counterpart, leaving 104 fields with more than one NIR galaxy identified as a possible counterpart. Of these 104 fields, a single counterpart could be ascertained for 46 fields, while the NIR counterpart for 58 fields remained ambiguous. Moreover, of the 317 fields with only one possible counterpart, we consider 303 to be confirmed based on visual inspection. The H I sources with no identified NIR counterpart are listed in Table 5.

The offsets between the H I and IRSF positions for the confirmed counterparts are plotted in Fig. 9. The large circle shows an offset of 4 arcmin, which is the pixel size of the H I data. 98 per cent of the detections lie within 4 arcmin and 88 per cent are within 3 arcmin. As a comparison, for the two parts of HIZOA Northern Extension (NE), Donley et al. (2005) confirm 54–60 per cent 2MASS counterparts within 3 arcmin. In their final counterpart selection, Donley et al. (2005) exclude counterparts offset by >4 arcmin as statistically unlikely. Our detection rate is slightly better than that of Donley et al. (2005) given that these NIR data are deeper than 2MASS and are better able to penetrate both the dust and stars of the Milky Way despite the fact that the NE fields lie at lower extinction and star density than much of the rest of the HIZOA fields.

Fig. 10 shows the spatial distribution of the 421 galaxies with identified counterparts and the 157 fields with no identified counterpart. For $\log(N_{(K_s<14\,\mathrm{mag})}/\mathrm{deg}^2) < 4.0$, nearly all galaxies have NIR detections. At stellar densities of $\log(N_{(K_s<14\,\mathrm{mag})}/\mathrm{deg}^2) > 4.5$, the detection of galaxies correlates strongly with the extinction level. The likelihood of a detection is clearly determined by the foreground stellar density and for a given stellar density decreases at higher extinction. The amount of non-detections increases slightly at intermediate stellar densities. At slightly higher stellar densities, $4.5 < \log(N_{(K_s<14\,\mathrm{mag})}/\mathrm{deg}^2) < 5.0$, most galaxies have NIR detections, except where the extinction level is very high ($A_{K_s} > 3.0$ mag). However, for very high star density, $\log(N_{(K_s<14\,\mathrm{mag})}/\mathrm{deg}^2) > 5.0$, almost no counterparts are found, i.e. a ZoA of only $\pm 2^\circ$ in latitude for the longitudes $\pm 60^\circ - 70^\circ$ around the Galactic bulge.

The Schlegel et al. (1998) foreground extinction of the detected galaxies, measured in the K_s band, ranges between 0.03 and 4.48 mag with a mean extinction of $\langle 0.41\mathrm{mag} \rangle$. Fig. 11 shows the number of galaxies detected and not detected as a function of foreground extinction in the K_s band. The distribution of detected and non-detected galaxies is also shown as a function of the stellar density in Fig. 11. The fraction of galaxies detected increases towards lower extinction and lower stellar density. However, two things are noteworthy: the overall distribution of non-detections is fairly flat in both plots, and hence nearly independent of foreground extinction or star density. These non-detections are most likely dwarfish blue low surface brightness galaxies that will not be picked up in any NIR survey, even far away from the Milky Way. Indeed, within the area with lower extinction and lower stellar density, the non-detections do on average have lower observed linewidths and H I masses than the H I sources with identified NIR counterparts. Moreover, the fraction of non-detections increases with decreasing H I linewidth and H I mass. Secondly, the areal fraction of high Galactic extinction and/or high star density is small (see also Fig. 10).

4.2 Magnitude and colour distribution

This section presents the magnitude and colour distributions of the 421 detected galaxies. Fig. 12 shows the distribution of the observed (dotted histogram) and extinction-corrected (solid histogram) $K_s = 20$ mag arcsec^{-2} fiducial isophotal magnitudes in J (blue), H (green) and K_s (red). The magnitudes are corrected

[6] 2MASX uses the peak J-band pixel while our photometry is based on the centroid of the super co-add image.

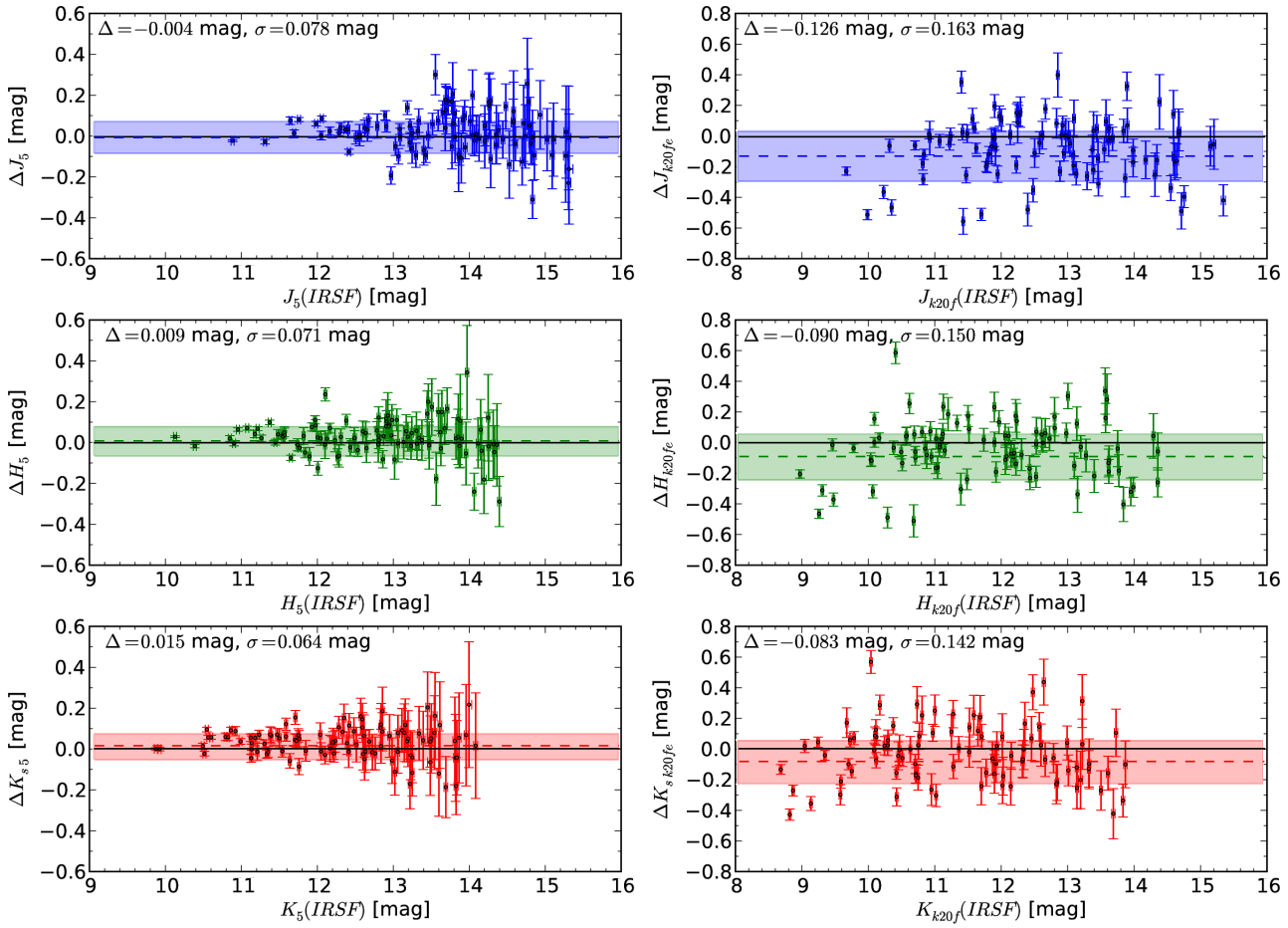

Figure 8. Comparison of the 5 arcsec circular aperture (left) and $K_s = 20$ mag fiducial isophotal (right) magnitudes in J (top), H (middle) and K_s (bottom) between the IRSF and 2MASX. The horizontal coloured strip shows the 1σ dispersion around the mean. In both figures, the horizontal coloured strip shows the 1σ dispersion around the mean (horizontal dashed line). The mean and standard deviation are given in the top-left corner of each plot.

Table 4. Comparison of 2MASX and IRSF/SIRIUS 5 arcsec aperture and $K_s = 20$ mag fiducial isophotal magnitudes.

Filter	5 arcsec aperture		$K_s = 20$ mag fiducial	
	$\langle\Delta m\rangle$ (mag)	σ (mag)	$\langle\Delta m\rangle$ (mag)	σ (mag)
J	−0.004	0.078	−0.13	0.16
H	0.009	0.071	−0.09	0.15
K_s	0.015	0.064	−0.08	0.14

for foreground extinction based on the DIRBE/*IRAS* maps,[7] scaled by the factor 0.87 derived in Section 5. The mean observed and extinction-corrected magnitudes are listed in Table 6; the mean extinction-corrected magnitudes are 0.80, 0.52 and 0.34 mag brighter than the mean observed magnitudes in J, H and K_s, respectively. For the NWS (conducted on the IRSF using the same observational strategy and data reduction), Riad (2010) determined magnitude completeness limits of $J = 16.6$, $H = 15.8$ and $K = 15.4$ mag and extinction-corrected isophotal magnitudes of $J^o = 15.6$, $H^o = 15.3$ and $K_s^o = 14.8$ mag in regions with dust obscuration below $A_{K_s} < 1.0$ mag and stellar densities less than $\log(N_{(K_s<14\,\mathrm{mag})}/\mathrm{deg}^2) = 4.71$.

The 5 arcsec aperture magnitudes are used to derive the NIR colours of the detected galaxies; the distribution of the observed colours is plotted in the *top* panel of Fig. 13 and that of the extinction-corrected colours in the *bottom* panel. $J - H$ is plotted in blue, $H - K_s$ in green and $J - K_s$ in red. The mean values of each colour are plotted as vertical dotted lines. It is evident that the distributions of observed colours are skewed towards the red end as a result of selective extinction. This is due to reddening by extinction. The extinction-corrected colour distributions are more symmetric and less dispersed. Table 7 lists the mean values of the observed and extinction-corrected colours as well as the dispersion of each distribution. For comparison, the mean colours of the 2MASS Large Galaxy Atlas (LGA), $\langle(J-H)^0\rangle = 0.73$ mag, $\langle(H-K)^0\rangle = 0.27$ mag and $\langle(J-K)^0\rangle = 1.00$ mag, are also given (Jarrett 2000; Jarrett et al. 2003). The mean extinction-corrected colours of $\langle(J-H)^0\rangle = 0.67$ mag, $\langle(H-K)^0\rangle = 0.24$ mag and $\langle(J-K)^0\rangle = 0.91$ mag are consistent with those of the LGA. We ignore the effects of morphological type on the distribution of the NIR colours and plot all the galaxies together. This is because we consider the majority of our galaxies to be of intermediate type (see Section 3.6), morphological types are harder to determine at low latitudes and because NIR colours are known to vary only slightly with morphological type (see Jarrett 2000, who plots the NIR colour

[7] We have not corrected the magnitudes for the changes in the isophotal shape due to extinction (see Riad, Kraan-Korteweg & Woudt 2010).

Table 5. H I sources with no likely NIR counterpart.

J0738−24	J0741−22	J0743−25A	J0746−35	J0755−38
J0758−36	J0817−29A	J0821−45	J0852−49	J0902−40
J0909−48B	J0912−53	J0917−48	J0927−49	J0928−50
J0931−43	J0939−56	J0945−48	J0947−54	J0949−49
J0950−52	J0951−53	J0957−58	J1000−58B	J1012−51
J1014−54	J1017−62	J1024−61	J1036−58	J1049−55
J1123−61	J1134−59	J1137−64	J1143−57	J1143−59
J1149−62	J1152−59	J1206−61	J1211−59	J1216−65
J1216−66	J1221−61	J1222−57	J1230−59	J1233−60
J1233−65	J1235−58	J1242−57	J1246−68	J1249−58
J1259−64	J1304−58	J1317−65	J1329−60	J1329−61
J1341−64	J1342−60	J1343−65	J1348−61	J1358−59
J1405−59	J1412−56B	J1414−56	J1414−62	J1415−62
J1416−55A	J1417−57	J1419−58A	J1419−64	J1422−57
J1423−59	J1424−60	J1426−55	J1426−60	J1427−65A
J1429−58	J1434−56B	J1438−60	J1441−62	J1442−57
J1447−57	J1452−55	J1452−57	J1501−59	J1504−57
J1511−60	J1513−56	J1522−52	J1522−61	J1528−52
J1530−58	J1531−52	J1531−55	J1534−56	J1535−54
J1536−56	J1539−57	J1539−59A	J1539−60	J1541−52
J1541−60	J1542−55	J1543−57	J1545−56	J1549−57
J1551−59	J1553−50	J1558−53	J1558−59	J1600−56
J1605−51	J1605−59	J1608−54	J1612−52	J1622−44A
J1622−53	J1622−54	J1629−42	J1632−29A	J1638−49
J1640−45	J1643−49	J1643−54	J1644−42B	J1653−44
J1656−44	J1704−41	J1705−29	J1714−44	J1719−37
J1719−48	J1721−37	J1727−41	J1727−49	J1728−43
J1739−24	J1739−51	J1749−32B	J1758−31	J1758−33
J1805−25	J1807−06	J1808−21	J1814−35	J1816−36
J1817−04	J1817−32	J1820+07	J1826−06	J1834−30
J1835−03	J1844−11	J1901+06	J1907−00	J1926+08
J1930+11	J1940+11			

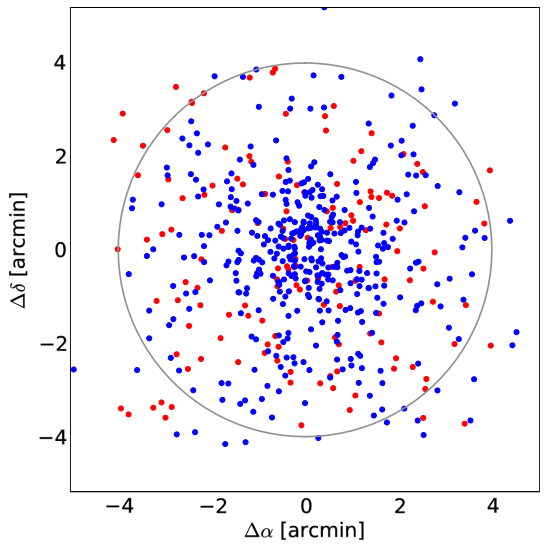

Figure 9. Positional offsets between H I positions and IRSF positions Confirmed counterparts are plotted in blue and unconfirmed counterparts in red. The large circle shows an offset of 4 arcmin, which is the pixel size of the H I data. 94 per cent of the confirmed detections lie within 4 arcmin and 77 per cent within 3 arcmin.

distributions for the LGA for different morphological types). The dispersion of the extinction-corrected colours of 0.1−0.2 mag is consistent with the dispersion in their distributions. The consistency between the mean values and dispersions of the extinction-corrected colours derived here and for the 2MASS LGA outside the ZoA adds credence to the new extinction correction derived in Section 5.

4.3 Usefulness for TF studies

For the 2MTF survey, Masters et al. (2008) have already determined template relations for the TF relation in the 2MASS J, H and K_s bands which can be used for these data. We show here that the quality of our photometry is sufficient to be used for TF distances and peculiar velocities and so will be helpful in filling in the 2MTF ZoA. The dominant errors driving that of the TF peculiar velocities are the absolute magnitude error, $\sigma_{\rm M}$, the velocity width error, $|b|\sigma_{\rm W}$ expressed in magnitudes, where b is the TF slope, and an intrinsic TF scatter term, $\epsilon_{\rm int}$. Neglecting the covariances between the first two values arising from inclination corrections, the quadrature sum is approximately the total measurement error. We comment briefly on each of these terms.

The absolute magnitude error is dominated by the measured apparent magnitude error, i.e. the errors in our photometry, as well as the error in the extinction correction. The measured errors in our magnitudes are typically ∼0.025 mag, and for a brighter sample ($K_s \leq 11.25$ mag, the same selection for the 2MTF galaxies), the error is more typically 0.02 mag. In comparison, the errors on the 2MASS galaxies are typically 0.1 and 0.06 mag for galaxies brighter than $K_s \leq 11.25$ mag. The I-band magnitude errors used in Springob et al. (2007) are typically <0.05 mag. For A_{K_s} up to 1 mag, we expect that the error in the extinction correction will be no larger than 0.04 mag (based on the 3 per cent error on our extinction correction factor in Section 5). We therefore conclude that the total magnitude error, under 0.1 mag, is less than or, in the worst case, of the same order of the 2MASS magnitudes being used for the 2MTF.

Since the velocity width error is determined largely by the accuracy of the linewidths, we do not expand on it here, except to note that it will be affected by the accuracy of the inclination determined from our photometry. Our ellipticity (i.e. axis ratio) errors are typically 0.06 which is better than the 0.1 error estimated by Masters et al. (2008) for the J-band axis ratio for 2MASS galaxies and comparable to the 0.04−0.06 for the I-band axis ratios (Springob et al. 2007).

Finally, from Masters et al. (2008), the intrinsic scatter in the TF relation varies between ∼0.15 and 1 mag across $2 < \log W < 2.8$.

5 NIR COLOURS AND EXTINCTION

The Schlegel et al. (1998) extinction maps derived from the DIRBE/*IRAS* data are not properly calibrated at low Galactic latitudes ($|b| < 5^\circ$). Foreground contaminating sources are not removed from these maps at $|b| < 5^\circ$ which can lead to an overestimate of the extinction. Moreover, Schlegel et al. (1998) assume an extinction law with $R_V \sim 3.1$, while the dust composition of giant molecular clouds within the Galactic disc is likely to differ from less dense dust clouds further from the Galactic plane. Thus, the extinction law and R_V parameter should vary across the Galactic plane. Higher density regions consisting of larger grains typically have $R_V \sim 5$. For these regions, the difference in extinction as a function of wavelength is lower (large grains are grey absorbers) and would also imply an overestimation of the total extinction for a given colour. Nevertheless, the DIRBE/*IRAS* maps remain the best available means to estimate the extinction in the ZoA. Moreover, several studies have shown that while they do indeed overestimate the extinction, it is possible to correct for this. For example, Nagayama et al. (2004) measured the colour excess of giant stars in a region around PKS

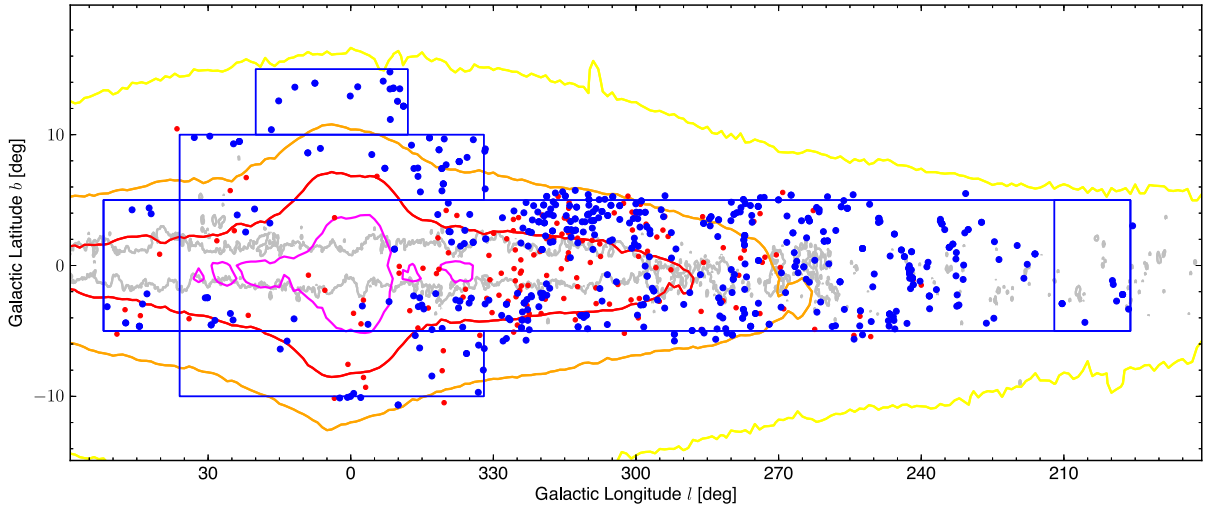

Figure 10. Spatial distribution of 578 detected and undetected possible NIR counterparts. The small red points show the 157 fields for which no counterpart was identified. The large blue points indicate the 421 fields in which one or more possible NIR counterparts for the H I source were identified. 2MASS PSC stellar density contours are overplotted with values of $\log(N_{(K_s<14\,\mathrm{mag})}/\mathrm{deg}^2) = 3.5$, 4.0, 4.5 and 5.0 plotted in yellow, orange, red and magenta, respectively. Very few detections are made at $\log(N_{(K_s<14\,\mathrm{mag})}/\mathrm{deg}^2) > 5.0$. An extinction contour is plotted in grey for $A_{K_s} = 3.0$ mag.

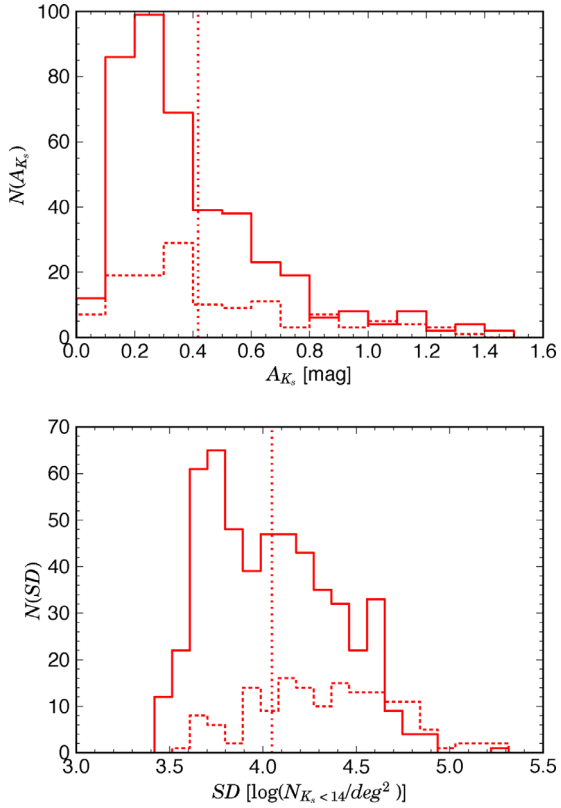

Figure 11. Top: number of fields with galaxies detected (solid line) and not detected (dotted line) as a function of K_s-band extinction. Only fields with $A_{K_s} < 1.5$ mag are included; 0.90 per cent of the detected galaxies have $A_{K_s} > 1.5$ mag. The vertical dotted line shows the mean extinction of ⟨0.41 mag⟩. Bottom: as above but as a function of stellar density. The vertical dotted line shows the mean stellar density of ⟨4.04 mag⟩.

1343−601 (l, $b = 309.^\circ7$, $1.^\circ7$) and found the Schlegel values to be 33 per cent too high. Schröder et al. (2007) looked at the $I - J$, $J - K_s$ and $I - K_s$ NIR colours of galaxies in the same region and concluded that the extinction is 87 per cent of the DIRBE values, i.e. the DIRBE values overestimate the extinction by 15 per cent. Other independent studies have shown the true extinction to be 67−87 per cent of the DIRBE values (Arce & Goodman 1999; Choloniewski & Valentijn 2003; Dutra et al. 2003; Schröder et al. 2005; van Driel et al. 2009). Furthermore, in their study of northern ZoA galaxies, van Driel et al. (2009) find that the overestimate depends on the amount of extinction, increasing from a factor of 0.86 for galaxies with B-band extinction in the range $2 < A_B < 6$, to a factor of 0.69 for the more heavily extincted galaxies with $6 < A_B < 12$. The consistency of their values with those derived in the southern ZoA suggests little or no variation with Galactic longitude.

Since the NIR colours are nearly independent of galaxy type, the NIR colours of nearby galaxies provide an independent means to determine the extinction at low latitudes. We apply an extinction correction based on the DIRBE/*IRAS* values and look for residuals in the resulting colours; the true extinction-corrected colours should be independent of extinction. Fig. 14 shows the extinction-corrected NIR colours, $(J - H)^o$, $(H - K_s)^o$ and $(J - K_s)^o$, as a function of the K_s-band extinction, A_{K_s}, for all NIR detections with reliable photometry in all three bands. The galaxies cover a wide range of Galactic latitude and longitude. The colours were determined from the 5 arcsec aperture magnitudes. The DIRBE/*IRAS* maps clearly overestimate the extinction at these low latitudes. The dashed lines show a linear least-squares fit to the data. There is a clear trend for the colours of galaxies at high extinction to be bluer than expected. The fits give

$$(J - H)^o = (-0.070 \pm 0.027)A_{K_s} + (0.675 \pm 0.013),$$

$$(H - K_s)^o = (-0.114 \pm 0.026)A_{K_s} + (0.270 \pm 0.013) \text{ and}$$

$$(J - K_s)^o = (-0.172 \pm 0.044)A_{K_s} + (0.943 \pm 0.021),$$

with an rms of 0.14, 0.13 and 0.21 mag, respectively.

Following the method first derived by Schröder et al. (2007), we assume that the Schlegel values, A_{K_s}, overestimate (underestimate) the true extinction, $\widetilde{A_{K_s}}$, by a constant multiplicative factor f, i.e.

$$\widetilde{A_{K_s}} = f A_{K_s}.$$

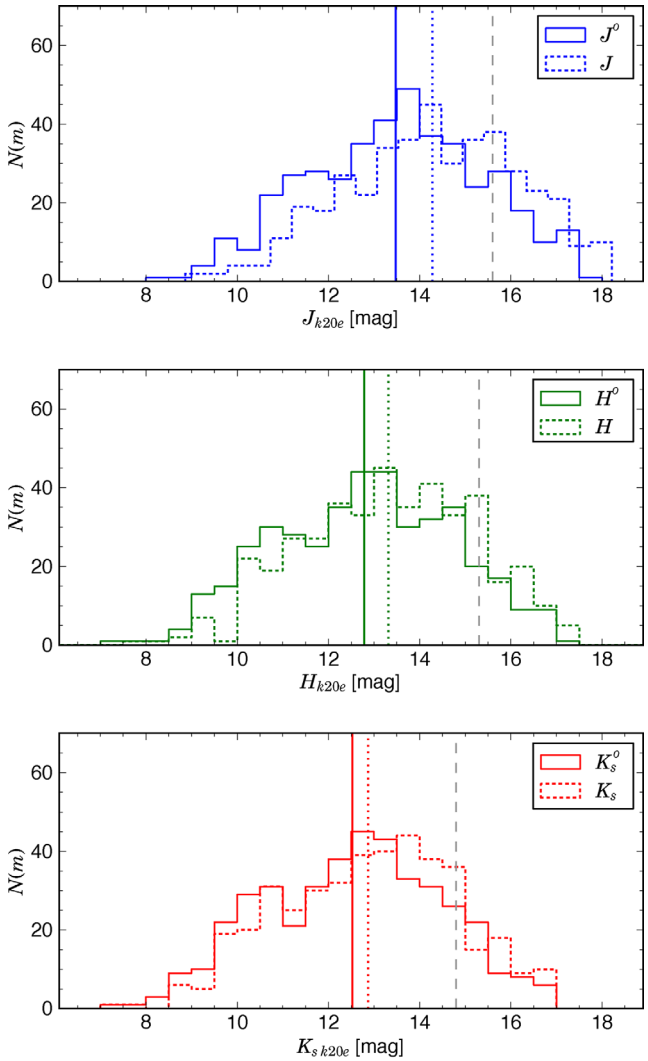

Figure 12. Distribution of $K_s = 20$ mag arcsec^{-2} fiducial isophotal magnitudes in J (top, blue), H (middle, green) and K_s (bottom, red) in 0.5 mag bins. The dotted histograms show the observed magnitudes and the filled solid histograms show the extinction-corrected magnitudes. The vertical dotted lines indicate the mean observed values and the vertical solid lines show the mean extinction-corrected magnitudes. The grey vertical dashed lines show the extinction-corrected completeness limits from Riad (2010).

Table 6. Mean observed and extinction-corrected $K_s = 20$ mag arcsec^{-2} fiducial isophotal magnitudes.

Filter	$\langle m \rangle$ (mag)	$\langle m^o \rangle$ (mag)
J	14.28	13.48
H	13.31	12.79
K_s	12.87	12.53

The correction factor is related to the slope of the linear fit by

$$f = a\left(\frac{E(C)}{A_{K_s}}\right)^{-1} + 1,$$

where $E(C)/A_{K_s}$ is the ratio of selective to total extinction which is obtained by integrating the extinction law of Cardelli et al. (1989) over each of the SIRIUS J, H and K_s bandpasses:

$$A_J = 0.863E(B-V),$$

$$A_H = 0.570E(B-V),$$

$$A_{K_s} = 0.368E(B-V).$$

From the linear fits, we derive

$$f_{(J-H)} = 0.913 \pm 0.030,$$

$$f_{(H-K_s)} = 0.793 \pm 0.042 \text{ and}$$

$$f_{(J-K_s)} = 0.784 \pm 0.046;$$

however, only two are independent. We choose to take the weighted mean of $f_{(J-H)}$ and $f_{(H-K_s)}$ as these colours are least affected by k-corrections (see e.g. Poggianti 1997) and have the smallest errors. Thus, we get

$$f = 0.87 \pm 0.03,$$

i.e. the true extinction is 13 per cent lower than that predicted by the DIRBE/*IRAS* values, averaging across the entire southern ZoA. This is consistent with the value of Schröder et al. (2007) in the region of PKS 1343−601 ($l, b = 309.^\circ7, 1.^\circ7$).

5.1 Discussion of possible sample biases

We investigate whether the observed dependence of colour on the extinction is a result of a selection effect or bias in our sample. We consider three effects.

(i) The loss of intrinsically red galaxies at higher extinction due to selective absorption near the completeness limit of the NIR observations. Adopting the magnitude limits of Riad (2010): 16.6, 15.8 and 15.4 mag in J, H and K_s, respectively, we calculate that a limit of 14.83 mag in the K_s band will be sensitive to $J-K$ colours within 0.5 mag of the mean value even with an extinction of A_{K_s} of 1.4 mag. Similarly a cut-off of 15.03 mag in K_s applies for the $H-K$ colours. Finally, for $J-H$, a cut-off of $H = 15.27$ allows us to detect galaxies with colours up to 0.5 mag from the mean with an extinction of $A_{K_s} = 1.5$ mag. After selecting sub-samples based on cut-offs of $K_s = 14.75$ mag for $J-K_s$ and $H-K_s$ and $H = 15.0$ mag for $J-H$, we find no significant changes in the observed relation between the Schlegel extinction-corrected colours and the extinction. Therefore, we are confident that this is not a result of the completeness of the sample.

(ii) The effect of redshift on NIR colours, i.e. the k-correction. Poggianti (1997) give small linear corrections with z which amount to <0.03 mag for our galaxies. Limiting the sample to only those galaxies with confirmed counterparts so their velocities are known and selecting only those with $4000 < v < 6000$ km s^{-1}, we purposefully select a sample that will exaggerate this effect. However, we derive similar correction values for this sub-sample, indicating that it is not the major contributor to the observed gradients in the colour–extinction relations.

(iii) Small variations in the intrinsic colours of the detected galaxies as a function of galaxy type. The $J-H$ colour drops from the nominal value of 1.0 to 0.7 mag towards later type galaxies (Sdm). To investigate this effect, we select from the H I confirmed

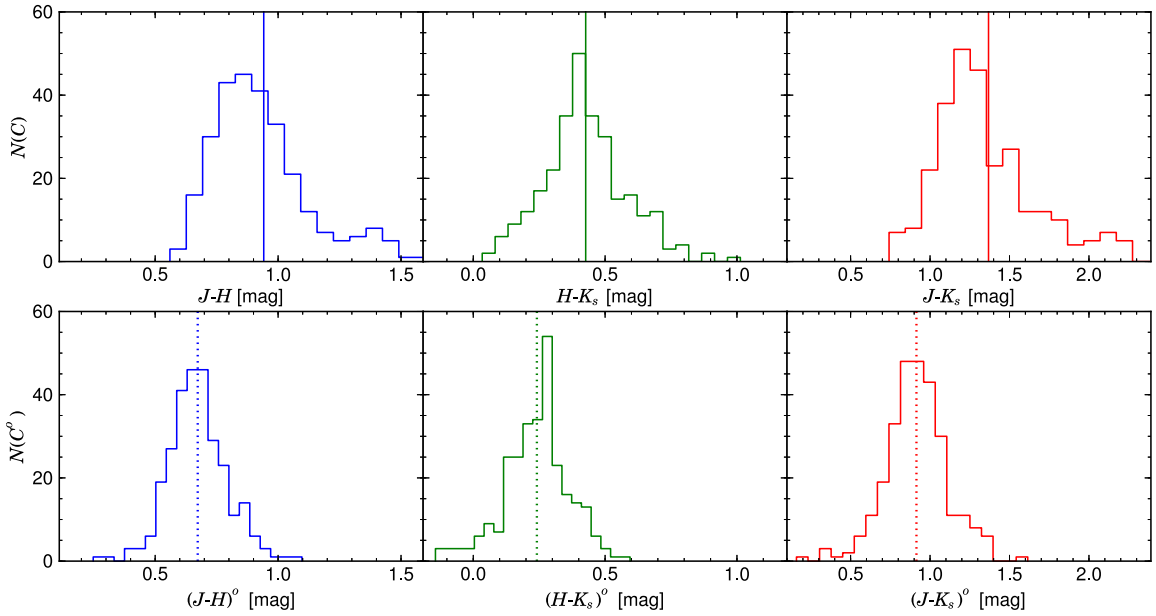

Figure 13. Histograms showing the distribution of NIR colours derived from the 5 arcsec aperture magnitudes. The top panel shows the observed colour distributions which are skewed to the right (redder) due to selective extinction. The bottom panel shows the extinction-corrected colour distributions which are more symmetric. $J - H$ is shown in blue, $H - K_s$ in green and $J - K_s$ in red. Vertical dotted lines indicate the mean values of each distribution.

Table 7. Mean observed and extinction-corrected colours.

Colour	$\langle C \rangle$ (mag)	σ_C (mag)	$\langle C^o \rangle$ (mag)	σ_{C^o} (mag)	$\langle C^o \rangle$ (LGA) (mag)
$J - H$	0.94	0.22	0.67	0.12	0.73
$H - K_s$	0.43	0.16	0.24	0.12	0.27
$J - K_s$	1.37	0.35	0.91	0.19	1.00

sample only those galaxies with inclination-corrected linewidths $\log W < 2.2$, which are likely to be later type Sdm galaxies. Again we find no significant difference in the derived correction factor. We further test this by using a sample of galaxies that are classed as later type based on visual inspection of the NIR images (T-types 4 and 5). There is no significant difference in the correction factor for this sample.

5.2 Variation with Galactic latitude and longitude

Because this sample covers such a large area along the southern Galactic plane, we can use it to investigate the extinction in different regions of the Galactic plane. In the following section, we determine the correction factor in several latitude and longitude bins.

Fig. 15 shows the extinction factor derived for several Galactic longitude and latitude bins. The size of the bins is restricted by the number of galaxies we have. Each bin contains 15−60 galaxies. For this case, we fit only the slope and keep the intercept fixed at the LGA values for the extinction-corrected NIR colours. We see no significant variation in the correction factor as a function of longitude or latitude. There is some variation within the errors. This is consistent with the results of van Driel et al. (2009), which suggest continuity of the overestimation across Galactic longitude. Initial work by Burstein and Heiles (see e.g. Heiles 1976; Burstein & Heiles 1978, 1982) suggested a variation with longitude based on the observed changes in the relationships between the H I gas-to-dust ratio and galaxy counts towards the Galactic bulge.

It is interesting to note that this 13 per cent lower DIRBE/*IRAS* extinction value nearly matches the value of 13 found by Schlafly et al. (2010) in a completely independent analysis of the blue tip of main-sequence turn-off stars, and that of 14 per cent found by Schlafly & Finkbeiner (2011) in a different analysis of the colours of stars with spectra in the Sloan Digital Sky Survey. Both studies are based on colours determined from other filter bands and in regions far away from the Galactic plane. Their comparable correction factors may well suggest that we have found the same effect, and this is in fact not induced by different dust properties at lowest Galactic latitudes.

6 SUMMARY

Deep NIR follow-up observations of HIZOA galaxies within 6000 km s^{-1} are presented. J, H and K_s images of 578 targets were obtained using the 1.4 m IRSF telescope with the SIRIUS camera. The combined three-colour NIR fields were visually searched for counterparts of the H I galaxies, and following the identification of possible counterpart galaxies, careful subtraction of foreground stars was done. Surface photometry was performed on the star-subtracted images to produce a photometric catalogue of 555 NIR galaxies. A range of photometric parameters are determined for each source and used to compile the final NIR catalogue; these include the ellipticity, position angle, isophotal magnitudes and extrapolated total magnitudes in all three NIR bands.

A comparison with 2MASX positions found no significant offset, with dispersions of the order of 0.6 and 0.4 arcsec for RA and Dec., respectively. The magnitudes at small apertures all agreed very well with dispersions of 0.07 mag. There was a slightly larger offset for $K_s = 20$ mag arcsec^{-2} fiducial isophotal magnitudes, which were fainter as derived from the IRSF photometry compared to 2MASX (−0.13, −0.09 and −0.08 mag for the three NIR bands). This conforms well with the expectations because of the improved star subtraction that is possible with the higher resolved images. The dispersion hovers around 0.15 mag when compared to 2MASX.

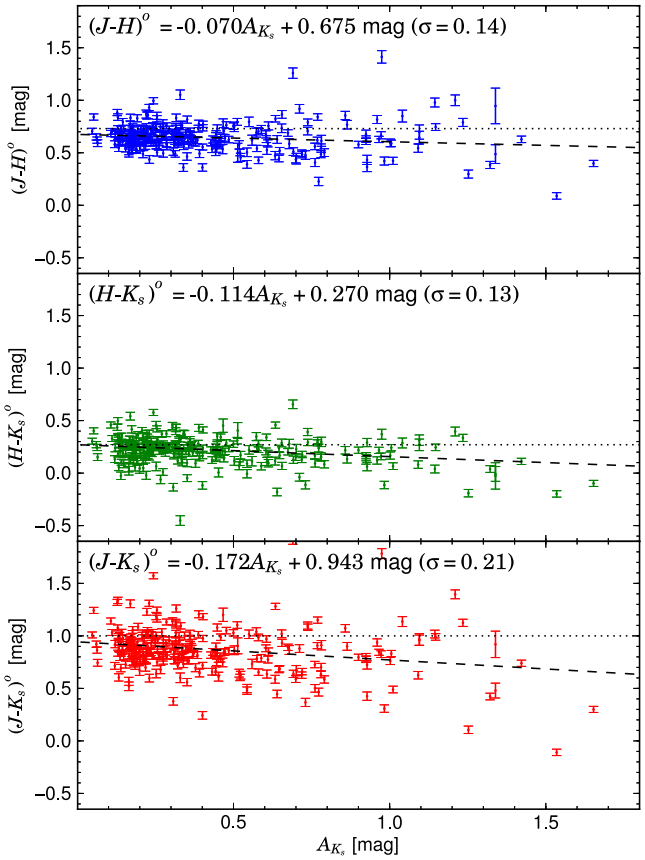

Figure 14. Extinction-corrected NIR colours plotted as a function of K_s-band extinction derived from the DIRBE/*IRAS* maps (Schlegel et al. 1998), from top to bottom: $(J - H)^o$ (blue), $(H - K_s)^o$ (green) and $(J - K_s)^o$ (red). The colours are corrected for extinction based on the Schlegel et al. (1998) maps and Cardelli, Clayton & Mathis (1989) extinction laws. The dashed lines in each panel show a least-squares linear fit to the colours and the fitted linear equation is given in the top-left corner. The dotted lines show the mean intrinsic NIR galaxy colours determined by Jarrett et al. (2003).

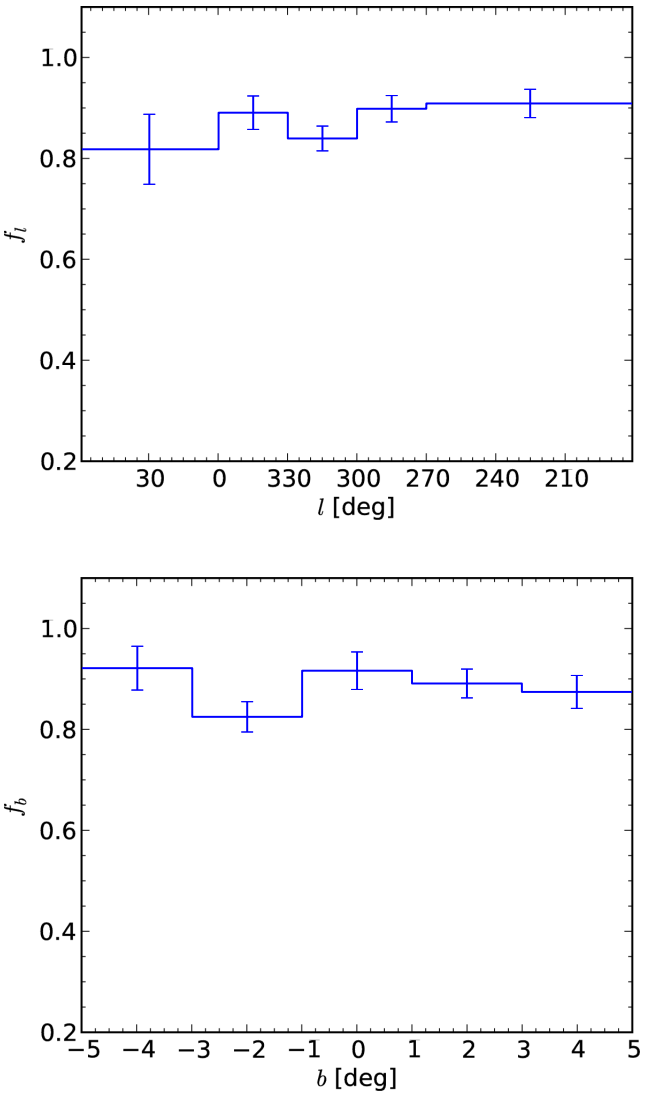

Figure 15. DIRBE/*IRAS* extinction correction factor as a function of Galactic longitude, l (top) and Galactic latitude, b (bottom).

This again is understood in that the deeper IRSF images will often allow a better recovery of extended low surface brightness discs of this spiral galaxy sample.

We have shown that the quality of the photometry is sufficient for use with the TF relation to determine distances and peculiar velocities. The expected magnitude errors are less than 0.1 mag and may be <0.05 mag in regions of lower extinction. The errors on the axis ratios are typically 0.06 which will not be prohibitive in determining inclinations for velocity width corrections.

The detection of NIR counterparts has proved quite successful. For $\log(N_{(K_s<14\,\mathrm{mag})}/\mathrm{deg}^2) < 4.0$, nearly all galaxies have NIR detections, though almost none are found for very high star density, $\log(N_{(K_s<14\,\mathrm{mag})}/\mathrm{deg}^2) > 5.0$, i.e. resulting in a ZoA of only $\pm 2^\circ$ in latitude for the longitudes $\pm 60^\circ - 70^\circ$ around the Galactic bulge. Within that higher stellar density range, the detection of galaxies correlates strongly with the extinction level. As shown with Fig. 10, most galaxies still have an NIR counterpart for $4.5 < \log(N_{(K_s<14\,\mathrm{mag})}/\mathrm{deg}^2) < 5.0$. However, this does not hold when the extinction level is very high ($A_{K_s} > 3.0$ mag). Overall, the deeper NIR follow-up imaging project of HIZOA galaxies observations shows a vast improvement compared to 2MASX, which recovered only 130 certain 2MASX counterparts for the full HIZOA catalogue of ∼1100 galaxies.

We have used the NIR colours of all the detected galaxies to investigate the extinction in the Galactic plane, to test whether the dust properties change at these high dust column densities. The ratio of the true extinction to the DIRBE/*IRAS* extinction (Schlegel et al. 1998) was found to be 0.87 across the whole HIZOA survey region. This value showed no significant variation with Galactic longitude and latitude. This value is completely compatible with the values found by Schlafly & Finkbeiner (2011) which were obtained based on an analysis of stellar data. The result here might be an independent confirmation, rather than being due to a difference in dust properties at low Galactic latitudes.

ACKNOWLEDGEMENTS

We acknowledge the HIZOA survey team for early access to the data. We thank the numerous observers that have helped with completing this survey and T. Jarrett and A. Schröder for insightful discussions on the surface photometry. We also thank the anonymous referee for helpful suggestions. The work of WLW was based on research generously supported by the South African SKA project. WLW, PAW and RKK acknowledge financial support from UCT

and the NRF. This work is based on observations obtained at the South African Astronomical Observatory.

REFERENCES

Aaronson M., Huchra J., Mould J., 1979, ApJ, 229, 1
Abate A., Feldman H. A., 2012, MNRAS, 419, 3482
Arce H. G., Goodman A. A., 1999, ApJ, 512, L135
Barnes D. G. et al., 2001, MNRAS, 322, 486
Bertin E., Arnouts S., 1996, A&AS, 117, 393
Bertschinger E., Dekel A., 1989, ApJ, 336, L5
Bilicki M., Chodorowski M., Jarrett T., Mamon G. A., 2011, ApJ, 741, 31
Bottinelli L., Durand N., Fouque P., Garnier R., Gouguenheim L., Paturel G., Teerikorpi P., 1992, A&AS, 93, 173
Burstein D., Heiles C., 1978, ApJ, 225, 40
Burstein D., Heiles C., 1982, AJ, 87, 1165
Buta R. J., McCall M. L., 1999, ApJS, 124, 33
Cardelli J. A., Clayton G. C., Mathis J. S., 1989, ApJ, 345, 245
Choloniewski J., Valentijn E. A., 2003, Acta Astron., 53, 265
Cluver M. E. et al., 2008, ApJ, 686, L17
Dekel A., 1994, ARA&A, 32, 371
Dekel A., Bertschinger E., Faber S. M., 1990, ApJ, 364, 349
Donley J. L. et al., 2005, AJ, 129, 220
Dutra C. M., Ahumada A. V., Clariá J. J., Bica E., Barbuy B., 2003, A&A, 408, 287
Erdoğdu P., Lahav O., 2009, Phys. Rev. D, 80, 043005
Feldman H. A., Watkins R., Hudson M. J., 2010, MNRAS, 407, 2328
Giovanelli R., Haynes M. P., Salzer J. J., Wegner G., da Costa L. N., Freudling W., 1994, AJ, 107, 2036
Heiles C., 1976, ApJ, 204, 379
Henning P. A., Kraan-Korteweg R. C., Staveley-Smith L., 2005, in Fairall A. P., Woudt P. A., eds, ASP Conf. Ser. Vol. 329, Nearby Large-Scale Structures and the Zone of Avoidance. Astron. Soc. Pac., San Francisco, p. 199
Huchra J. P. et al., 2012, ApJS, 199, 26
Hudson M. J., Smith R. J., Lucey J. R., Branchini E., 2004, MNRAS, 352, 61
Jarrett T. H., 2000, PASP, 112, 1008
Jarrett T. H., Chester T., Cutri R., Schneider S. E., Strutskie M., Huchra J. P., 2000, AJ, 119, 2498
Jarrett T. H., Chester T., Cutri R., Schneider S. E., Huchra J. P., 2003, AJ, 125, 525
Kashlinsky A., Atrio-Barandela F., Ebeling H., Edge A., Kocevski D., 2010, ApJ, 712, L81
Kirby E. M., Jerjen H., Ryder S. D., Driver S. P., 2008, AJ, 136, 1866
Kochanek C. S. et al., 2001, ApJ, 560, 566
Kolatt T., Dekel A., Lahav O., 1995, MNRAS, 275, 797
Kraan-Korteweg R. C., 2005, Rev. Mod. Astron., 18, 48
Kraan-Korteweg R. C., Lahav O., 2000, A&AR, 10, 211
Lahav O., Fisher K. B., Hoffman Y., Scharf C. A., Zaroubi S., 1994, ApJ, 423, L93
Lavaux G., Hudson M. J., 2011, MNRAS, 416, 2840
Lavaux G., Tully R. B., Mohayaee R., Colombi S., 2010, ApJ, 709, 483
Loeb A., Narayan R., 2008, MNRAS, 386, 2221
Lynden-Bell D., Faber S. M., Burstein D., Davies R. L., Dressler A., Terlevich R. J., Wegner G., 1988, ApJ, 326, 19
Lynden-Bell D., Lahav O., Burstein D., 1989, MNRAS, 241, 325
Macaulay E., Feldman H., Ferreira P. G., Hudson M. J., Watkins R., 2011, MNRAS, 414, 621
Masters K. L., Springob C. M., Haynes M. P., Giovanelli R., 2006, ApJ, 653, 861
Masters K. L., Springob C. M., Huchra J. P., 2008, AJ, 135, 1738
Nagashima C. et al., 1999, in Nakamoto T., ed., Proceedings of Star Formation Development of SIRIUS – A Simultaneous-Color InfraRed Imager for Unbiased Survey. Nobeyama Radio Observatory, Japan, p. 397
Nagayama T. et al., 2003, in Iye M., Moorwood A. F. M., eds, Proc. SPIE Vol. 4841, Instrument Design and Performance for Optical/Infrared Ground-based Telescopes. SPIE, Bellingham, p. 459
Nagayama T. et al., 2004, MNRAS, 354, 980
Nagayama T. et al., 2006, MNRAS, 368, 534
Nusser A., Davis M., 2011, ApJ, 736, 93
Poggianti B. M., 1997, A&AS, 122, 399
Radburn-Smith D. J., Lucey J. R., Woudt P. A., Kraan-Korteweg R. C., Watson F. G., 2006, MNRAS, 369, 1131
Riad I. F., 2010, PhD thesis, University of Cape Town
Riad I. F., Kraan-Korteweg R. C., Woudt P. A., 2010, MNRAS, 401, 924
Schlafly E. F., Finkbeiner D. P., 2011, ApJ, 737, 103
Schlafly E. F., Finkbeiner D. P., Schlegel D. J., Jurić M., Ivezić Ž., Gibson R. R., Knapp G. R., Weaver B. A., 2010, ApJ, 725, 1175
Schlegel D. J., Finkbeiner D. P., Davis M., 1998, ApJ, 500, 525
Schröder A. C., Kraan-Korteweg R. C., Mamon G. A., Woudt P. A., 2005, in Fairall A. P., Woudt P. A., eds, ASP Conf. Ser. Vol. 329, Nearby Large-Scale Structures and the Zone of Avoidance. Astron. Soc. Pac., San Francisco, p. 167
Schröder A. C., Mamon G. A., Kraan-Korteweg R. C., Woudt P. A., 2007, A&A, 466, 481
Shafi N., 2008, Master's thesis, University of Cape Town
Skelton P., 2007, Master's thesis, University of Cape Town
Skelton R. E., Woudt P. A., Kraan-Korteweg R. C., 2009, MNRAS, 396, 2367
Springob C. M., Masters K. L., Haynes M. P., Giovanelli R., Marinoni C., 2007, ApJS, 172, 599
Strutskie M. F., 2006, AJ, 131, 1163
Tabur V., 2007, Publ. Astron. Soc. Aust., 24, 189
Theureau G., Hanski M. O., Coudreau N., Hallet N., Martin J., 2007, A&A, 465, 71
Tokunaga A. T., Simons D. A., Vacca W. D., 2002, PASP, 114, 180
Tully R. B., Fisher J. R., 1977, A&A, 54, 661
Tully R. B., Fisher J. R., 1987, Atlas of Nearby Galaxies. Cambridge Univ. Press, Cambridge
van Driel W., Schneider S. E., Kraan-Korteweg R. C., Monnier Ragaigne D., 2009, A&A, 505, 29
Watkins R., Feldman H. A., Hudson M. J., 2009, MNRAS, 392, 743
Yahil A., Strauss M. A., Davis M., Huchra J. P., 1991, ApJ, 372, 380

SUPPORTING INFORMATION

Additional Supporting Information may be found in the online version of this article:

Table 3. Selected measured galaxy parameters for the 40 brightest K_{s20} magnitude galaxies in the catalogue (http://mnras.oxfordjournals.org/lookup/suppl/doi:10.1093/mnras/stu1155/-/DC1).

Please note: Oxford University Press is not responsible for the content or functionality of any supporting materials supplied by the authors. Any queries (other than missing material) should be directed to the corresponding author for the paper.

This paper has been typeset from a TEX/LATEX file prepared by the author.